



# FRINGE PROJECTION METHOD FOR TOPOGRAPHY AND DYNAMIC DEFORMATION MEASUREMENT

Thesis presented by:

**Ing. Andrea León Huerta**

in partial fulfillment of the requirements for the degree of  
Master of Science in Optics.

Advisor: Dra. Amalia Martínez García

December 2008  
León, Gto. México

# ABSTRACT

The thesis deals with the application of the fringe projection method for topography and dynamic deformation measurement. In the first part, we present an analysis of the influence of the grating period used in fringe projection technique for topography measurement. The algorithm used to the processing of the fringe images is phase shifting technique. Most phase shifting algorithms are developed for a signal without harmonics, i.e., a perfect sinusoidal signal. When they are used for phase detection of a nonsinusoidal signal there is an error in the results. In order to determine the grating period influence, sinusoidal fringes with different pitch are projected on a semi-spherical object. It is observed that some fringe patterns captured by the CCD camera have nonsinusoidal profile. These fringes are used to retrieve the surface topography. An error is evaluated by the comparison of the results with a reference surface which it was measured with the spherometer.

In the second part, it realized a monitoring by fringe projection technique of the deformation in sheet metal samples during a tensile test. Since it is a dynamic event, the use of Fourier transform method allows us to measure in real-time the deformation of the sample respect to its initial state, i.e., before applying the load. It is showed that the resolution of fringe projection technique is enough to detect the transition zone to predict failure. Study of material behavior is important due to the development of new materials that can exhibit an unexpected behavior.

*Dedicated to*  
*My family,*  
*Fernando and my daughter.*

## ACKNOWLEDGMENTS

This thesis work would not have been possible without the financial support of the Consejo Nacional de Ciencia y Tecnología (CONACyT) and Consejo Nacional de Ciencia y Tecnología del Estado de Guanajuato (CONCyTEG).

I would like to acknowledge the support and encouragement of my advisor Dra. Amalia Martínez and her invaluable supervision of this thesis.

I thank to the members of my dissertation jury: Dr. Cruz Meneses and Dr. Francisco Cuevas for evaluating this work and their valuable comments and suggestions that contributed to improvement of its quality.

I would like to thank Eng. Juan Antonio Rayas for his comments and suggestions and his invaluable help in laboratory.

I thank Dr. Daniel Malacara, for everything I learned from him. I owe a word of thanks to Dr. Ascencion Guerrero, Dr. David Moreno, Dr. Julio Cesar Estrada and Math. Guillermo Garnica for their help.

I acknowledge the support of Centro de Investigaciones en Optica, specially the attention that I received from Dirección de Formación Académica.

I thank everyone who gave me their friendship.

I would also thank to my family, especially to my mom and my aunt Carmen.

Finally, I especially thank Fernando for his constant patient, support and love.

# CONTENT

<b>INTRODUCTION</b>	<b>1</b>
<b>1 MECHANICAL ASPECTS</b>	<b>7</b>
1.1 ANALYSIS OF STRESS.....	7
1.2 ANALYSIS OF STRAIN.....	9
1.2.1 Relations between stress and strain.....	9
1.3 STRESS-STRAIN DIAGRAM.....	10
1.4 STRESS CONCENTRATION.....	12
REFERENCES.....	15
<b>2 MOIRÉ AND FRINGE PROJECTION TECHNIQUES</b>	<b>17</b>
2.1 MATHEMATICAL DESCRIPTION.....	18
2.2 IN-PLANE DIPLACEMENTS.....	21
2.3 OUT-OF-PLANE DISPLACEMENTS.....	23
2.3.1 Shadow moiré.....	23
2.3.2 Projection moiré.....	26
2.3.3 Fringe projection.....	27
2.3.4 Reflection moiré.....	29
REFERENCES.....	30
<b>3 PHASE MEASUREMENT</b>	<b>32</b>
3.1 PHASE SHIFTING.....	34
3.2 FOURIER TRANSFORM METHOD.....	36
3.3 PHASE UNWRAPPING.....	38
3.3.1 Unwrapping consistent phase maps.....	39
3.3.2 Unwrapping inconsistent phase maps.....	40
REFERENCES.....	42

<b>4 ANALYSIS OF GRATING PERIOD IN FRINGE PROJECTION TECHNIQUE</b>	<b>44</b>
4.1 INTRODUCTION.....	45
4.2 EXPERIMENT.....	47
4.3 CONCLUSION.....	54
REFERENCES.....	54
 <b>5 DYNAMIC MEASUREMENT OF OUT-OF-PLANE DEFORMATION IN TEST SPECIMEN BY FRINGE PROJECTION</b>	 <b>55</b>
5.1 INTRODUCTION.....	55
5.2 EXPERIMENT.....	57
5.3 CONCLUSION.....	68
REFERENCES.....	68
 <b>6 FINAL CONCLUSIONS</b>	 <b>69</b>
 <b>APPENDIX A: SPHEROMETER</b>	 <b>71</b>
REFERENCES.....	72
 <b>APPENDIX B: FRINGE EXTRAPOLATION</b>	 <b>73</b>
REFERENCES.....	74
 <b>APPENDIX C: LIST OF WORKS PRESENTED IN MEETINGS</b>	 <b>75</b>

# LIST OF FIGURES

## CHAPTER 1

Figure 1.1 A) Stress components on an infinitesimal element, and B) Displacement of line elements .	8
Figure 1.2 Deformation of a homogeneous, isotropic specimen under uniaxial load.	10
Figure 1.3 Stress-strain diagram.	11
Figure 1.4 Stress distribution for a uniform cross section.	12
Figure 1.5 Stress concentration effects due to a crack in: A) infinite and B) finite width plate.	13
Figure 1.6 Stress concentration factor $K$ for a flat bar with centrally located hole in tension.	13
Figure 1.7 Stress distribution in a nonuniform cross section. A) Non uniform cross section, B) Stress distribution below the yield point, C) Maximum stress over yield point, and) All fibers at the yield point.	14
Figure 1.8 The small circle represents load that must be redistributed, resulting in a larger plastic zone.	15

## CHAPTER 2

Figure 2.1 Moiré pattern between two overlap gratings of the same pitch at an angle $\theta$ .	19
Figure 2.2 Moiré patterns formed by: A) Two gratings of different pitches and no tilt, B) Two gratings of different pitches and tilted.	20
Figure 2.3 A three-dimensional displacement.	21
Figure 2.4 Geometry of shadow moiré with: A) illumination and viewing at infinity, B) illumination and viewing at finite distances.	24
Figure 2.5 Geometry of projection moiré.	26
Figure 2.6 Projected fringes on an object.	28
Figure 2.7 Geometry of fringe projection with uncollimated light.	29
Figure 2.8 Reflection moiré.	30

## CHAPTER 3

Figure 3.1 Phase modulation and detected signal for: A) integrating-bucket, and B) phase-stepping.....	34
Figure 3.2 A) Separated Fourier spectrum of a fringe pattern, B) Single spectrum selected and translated to the origin.....	37
Figure 3.3 A) Example of a wrapped phase, and B) the unwrapped phase after remove discontinuities.....	38
Figure 3.4 Path followed by the proposed algorithm.....	40
Figure 3.5 Example of a simple connected region containing valid phase data.....	40

## CHAPTER 4

Figure 4.1 Contrast of a detected signal for a finite size of integration. The upper line is for small integration interval, and the lower line for large integration interval. A) $f_s > f_{max}$ , B) $f_s = f_{max}$ , C) $f_s < f_{max}$ and D) $f_s \ll f_{max}$ .....	46
Figure 4.2 Distortion of two signals of equal period, $p=4 \text{ pix/fringe}$ , and a phase shift between them.....	47
Figure 4.3 Distortion of a signal with period: A) $p=8$ and B) $p=16 \text{ pix/fringe}$ .....	48
Figure 4.4 Experimental set up for three-dimensional shape measurement: 1. Projector, 2. Object, 3. CCD camera, and 4. PC.....	49
Figure 4.5 Schematic diagram of the experimental set up.....	49
Figure 4.6 Profile of projected fringes on the object surface, for a projected grating of periods: A) $p_1=4$ , B) $p_2=8$ , and C) $p_3=12$ , D) $p_4=16$ and E) $p_5=20 \text{ pix/fringe}$ .....	50
Figure 4.7 A) Wrapped phase and B) Three-dimensional shape, for grating period $p_2=8 \text{ pix/fringe}$ .....	52
Figure 4.8 Comparison between topography obtained by fringe projection against the reference surface which was measured with a spherometer. The period of the projected gratings is: A) $p_1=4$ , B) $p_2=8$ , C) $p_3=12 \text{ pix/fringe}$ , D) $p_4=16$ , and E) $p_5=20 \text{ pix/fringe}$ , respectively.....	53



## CHAPTER 5

Figure 5.1 A) Specimen dimensions in mm, and B) Stress-strain diagram obtained from the tensile test.....	57
Figure 5.2 A) Experimental setup: 1. Projector, 2. CCD camera, 3. Testing machine and specimen and 4. PC,.....	58
Figure 5.3 Fringe pattern, wrapped phase and deformation of the SS specimen during tensile test: A) beginning the test, B) elastic zone, C) plastic zone, D) necking, E) before fracture, and F) fracture.....	60
Figure 5.4 Fringe pattern, wrapped phase and deformation of the HRS C12 specimen during tensile test: A) beginning the test, B) elastic zone, C) plastic zone, D) necking, E) crack formation, F, G) fracture progression, and H) fracture.....	62
Figure 5.5 Fringe pattern, wrapped phase and deformation of the HRS C10 specimen during tensile test: A) beginning the test, B) elastic zone, C) plastic zone, D) necking, E) crack formation, F, G) fracture progression, and H) fracture.....	65

## APPENDIX A

Figure A.1 Three-leg spherometer.....	71
Figure A.2 Ring spherometer.....	72

## APPENDIX B

Figure B.1 A) Fringe pattern from a drilled specimen, B) Binary mask, C) Full-field fringe pattern obtained from fringe extrapolation.....	74
--	----

## LIST OF TABLES

Table 4.1 Error of the topography obtained.....	52
---	----

Table 5.1 Specimen specifications.....	57
--	----

## INTRODUCTION

Nowadays there is an increasing need for accurately measuring the three-dimensional (3D) shape of objects, as well as stress-strain and vibration measurements for a wide variety of applications. For this purpose there are both mechanical and optical techniques. Optical techniques offer the advantage of provide non-contact and full-field measurements of in-plane and out-of-plane components of displacements.

For out-of-plane measurements some optical techniques have been developed, such as: time-of-flight method [1], laser scanning [1], moiré methods [2], interferometry [3], photogrammetry [1], fringe projection [2], electronic speckle pattern interferometry (ESPI) [4, 5], Talbot interferometry [6] and moiré deflectometry [7, 8]. Each one offers different resolution, accuracy and limitations.

In the development of this thesis we select fringe projection technique to measure both, deformation and shape. This technique is related with projection moiré, but shape is directly decoded from the deformed fringe pattern recorded from the surface of a diffuse object without using a reference grating to create moiré fringes [1], and has the advantage of being easy to implement. Data acquisition is made in three steps: 1) phase detection, 2) phase unwrapping and 3) phase-to-depth conversion using the parameters of the optical system, all of which are involved in the sensitivity vector, thus obtaining dimensions of topography of the object analyzed in real coordinates [9].

Accuracy of the measurements is a relevant topic, unfortunately it is affected by many factors. We will describe some problems that arise when it is applied fringe projection method. Camera calibration is a crucial problem for computer vision where many tasks require the computation of accurate metric images. Calibrating a camera consists in determining the transformation which 3D points of a certain scene or object into their corresponding two dimensional (2D) projections onto the image plane of the camera. The precision of 3D reconstruction will be influenced by the veracity and reliability of camera and projector in the

system. Therefore, the lens distortion of camera and projector should be considered during calibration. Many techniques and some studies concerning calibration for lens distortion have been presented in the last years [10-13].

Barrel distortion occurs when the magnification at the center of the lens is greater than at the edges. A higher quality lens can be used to correct for this but this comes at additional cost to the image capture system. Barrel distortion is primarily radial in nature, with a relatively simple one parameter model accounting for most of the distortion. A cost effective alternative to an expensive lens is to algorithmically correct for the distortion using field programmable gate arrays.

When testing large surfaces telecentric systems are not convenient since the size of the measured field is limited by the diameter of optical system [2]. If the projection system is not telecentric the projected lines of the grating are not equidistant in the reference plane. Contouring surfaces are thus no longer flat. There are several ways of contouring this effect: making a special projection grating whose projection in the reference plane will give equispaced lines [14]. Others authors found an equation which considers that the fringe period is not constant and that depends on  $x$  [15-17].

Because of the finite distances there is also distortion due to viewing perspective. A point  $P$  on the surface will be apparently at  $P'$  when viewed through the grating. By simple geometry the actual coordinates  $(x_r, y_r)$  could be obtained from the measured coordinates  $(x_a, y_a)$ : this enables the measured surface to be mapped to the actual surface to correct for the viewing perspective [18].

Other parameter that will affect the topography measurement it is that the observed waveforms such as fringes in an interferogram often become nonsinusoidal because of, for example, the nonlinearity of the detector or the nonlinear of the projector which cause the projected fringe patterns to be nonsinusoidal, which results in phase error and therefore measurement error [19, 20].

System calibration techniques have been developed to obtain the mapping relationship between the phase distribution and the 3D object surface coordinates, without explicitly determining the system-geometry parameters. Instead, calibration parameters, which implicitly account for the system-geometry, are determined [21, 22]. In the calibration method, a plane is positioned successively at different positions from the camera. Usually, a marked point on the first calibration plane is used as the origin of the world reference system, then the following calibration results, a precise linear z stage has to be used. The main drawback of the system comes from practical limitations, such as its plane position restriction or the difficulty of calibrating big measurement volumes.

We analyze the influence of the nonsinusoidal profile of the fringes in shape measurement, by contouring an object with different grating periods.

Deformation measurements have to be made by obtaining a fringe pattern of the object in its original state and in its deformed state, followed by reconstruction of the object shape from these fringe patterns and finally by calculating the difference between these two measurements. We follow the changes induced in the topography of metallic sample sheets subjected to uniaxial tensile tests. A reference fringe pattern of the object before applying the load allows us to obtain deformation in real-time.

The organization of this thesis is described below:

**Chapter 1. Mechanical aspects:** some basic concepts of mechanics related with this thesis are presented.

**Chapter 2. Moiré and fringe projection techniques:** it is presented a description of moiré and fringe projection techniques.

**Chapter 3. Phase measurement:** it is presented a description of phase detection techniques, such as phase shifting and Fourier transform method, and phase unwrapping techniques.

**Chapter 4. Analysis of grating period in fringe projection technique:** it is presented an analysis of the error caused by a nonsinusoidal fringe profile. The shape of an object is obtained by fringe projection technique by using different grating periods. The comparisons of the topography obtained for each grating period with respect to reference surface, allows us to establish an appropriate grating period that minimizes the error in the measurement.

**Chapter 5. Dynamic measurement of out-of-plane deformation in test specimen by fringe projection:** deformation measurements in real-time of sheet metal specimens subjected to uniaxial tensile test are presented. By monitoring the entire process we detect the material behavior in the elastic and plastic zone during its elongation until fracture took place, which allows us to establish a comparison between different materials.

**Chapter 6. Final conclusions:** finally the obtained results and possible applications are reported.

**Appendix A. Spherometer:** a brief description of a spherometer and parameters used to determine the radius of curvature are presented.

**Appendix B. Extrapolation of fringes:** a description of a method used in processing of non full-field fringe patterns is explained. The fringes are extrapolated to apply the Fourier transform method. With this implementation in the method, errors in phase detection are avoided.

**Appendix C. List of works presented in meetings.**

## REFERENCES

1. Chen F., Brown G.M., Song M., "Overview of Three-Dimensional Shape Measurement Using Optical Methods", *Opt. Eng.*, **39**, pp. 10-22 (2000)
2. Paturski K., *Handbook of the Moiré Fringe Technique*, Elsevier, Amsterdam (1993)

3. Malacara D., *Optical Shop Testing*, Wiley, New York (1991)
4. Leendertz J.A., "Interferometric Displacement Measurement on Scattering Surfaces Utilizing Speckle Effect ", *J. Phys. E*, **3**, pp. 214-219 (1970)
5. Joenathan C., Pfister B., Tiziani H.J., "Contouring by Electronic Speckle Pattern Interferometry Employing Dual Beam Illumination", *Appl. Opt.*, **29**, pp. 1905-1911 (1990)
6. Rodriguez-Vera R., Kerr D., Mendoza-Santoyo F., "3-D Contouring of Diffuse Objects by Talbot-Projected Fringes", *J. of Mod. Opt.*, **38**, pp. 1935-1945 (1991)
7. Servin M., Rodriguez-Vera R., Carpio M., "Automatic Fringe Detection Algorithm Used for Moiré Deflectometry", *Appl. Opt.*, **29**, pp. 3266-3270 (1990)
8. Rottenkolber M., Podbielska H., "Measuring Ophthalmologic Surfaces by Means of Moiré Deflectometry", *Opt. Eng.*, **35**, pp. 1124-1133 (1996)
9. Martínez Amalia, Rayas J.A., Flores M.R., "Técnicas Ópticas para el Contorneo de Superficies Tridimensionales", *Rev. Mex. Fís.*, **51**, pp. 431-436 (2005)
10. Zhang Z., "Flexible Camera Calibration by Viewing a Plane From Unknown Orientation", *7th IEEE Int. Conf. Comput. Vis.*, pp 666-673 (1999)
11. [http://www.vision.caltech.edu/bouguetj/calib\\_doc/index.html](http://www.vision.caltech.edu/bouguetj/calib_doc/index.html)
12. Gribbon K.T., Johnston C.T., Bailey D.G., "A Real-Time FPGA Implementation of a Barrel Distortion Correction Algorithm with Bilinear Interpolation", *Proc. Image and Vision Computing NZ*, pp. 408-413 (2003)
13. Rayas J.A., Puga H.J., Martinez Amalia, "Efecto de la Calibración de una Cámara CCD Utilizada en un Sistema de Proyección de Franjas", *III Encuentro Participacion de la Mujer en la Ciencia*, ISBN 968-9241-02-8 (2006)
14. Yatagai T., Idesawa M., "Use of Synthetic Deformed Grating in Moiré Topography", *Opt. Commun.*, **20**, pp. 243-245 (1977)
15. Gasvik K.J., *Optical Metrology*, pp. 180-186, Wiley, England (2002)
16. Gasvik K. J., "Moiré Technique by Means of Digital Image Processing", *Appl. Opt.*, **22**, pp. 3543-3548 (1983).
17. Gasvik K. J., Fournery M. E., "Projection Moiré Using Digital Video Processing: A Technique for Improving the Accuracy and Sensitivity", *Transactions of the ASME*, **53**, pp. 652-656 (1986)
18. González R., Woods R.E., *Procesamiento Digital de Imagenes*, Chap. 2: Fundamentos de

la imagen digital, Addison-Wesley/Díaz de Santos, México (2002)

19. Hibino K., Oreb B.F., Farrant D.I., "Phase Shifting for Nonsinusoidal Waveforms with Phase-Shift Errors", *J. Opt. Soc. Am. A*, **12**, pp. 761-768 (1995)
20. Zhang S., Yau S., "Generic Nonsinusoidal Phase Error Correction for Three-Dimensional Shape Measurement Using Digital Video Projector", *Appl. Opt.*, **46**, pp. 36-43 (2007)
21. Cuevas F.J., Servin M., Rodríguez-Vera R., "Depth Object Recovery Using Radial Basis Functions", *Opt. Commun.*, **163**, pp. 270-277 (1999)
22. Jia P., Kofman J., English C., "Comparison of Linear and Nonlinear Calibration Methods for Phase-Measuring Profilometry", *Opt. Eng.*, **46**, 043601-043601-10 (2007)



# CHAPTER 1

## MECHANICAL ASPECTS

---

The mechanics of materials studies the behavior of a solid material under external forces applied to a body. The response of a material to external forces depends on their mechanical properties. Mechanical properties are described in terms of the types of force or stress that the material must withstand and how these are resisted. The most common properties are strength, hardness, ductility, and impact resistance, to determine these properties the material has to be submitted to different tests. Design engineers select a material based on its mechanical properties, and determine the range of usefulness and establish the service that can be expected to ensure safety during operation.

In this chapter we describe the basic terms to easily understand the behavior of a material subjected to external forces. Section 1.1 deals with the definition of stress. In Section 1.2 we describe strain and how it is related to stress. Section 1.3 describes a tensile test. Finally, in Section 1.4 we emphasize the mechanical behavior of a specimen during tensile loading.

### 1.1 ANALYSIS OF STRESS

When a body is subjected to the actions of external forces, the effects are transmitted through the material. Internal forces are thus produced to maintain the equilibrium. At each point of the body the intensity of internal forces varies. Stress is used to describe the distribution of a force over the area on which it acts. The stress at a small elementary area  $dA$  of the force  $dF$  transmitted across it, is given by:

$$s = \frac{dF}{dA} \quad (1.1)$$

which is composed of the normal stress  $\sigma$  and the shear stress  $\tau$ .

The normal stress represent the average stress over a transversal section:

$$\sigma = \frac{F_n}{A} \quad (1.2)$$

and requires a single subscript which indicates the direction in which it acts.

The shear stress is a stress applied tangential to the transversal section:

$$\tau = \frac{F_t}{A} \quad (1.3)$$

and requires two subscript, the first one indicated by the direction on its normal the plane on which the shear stress acts while the second indicates the direction of the shear stress in that plane.

The description of the complete stress state tensor at a point requires three planes to define the stress tensor [1, 2], Figure 1.1A:

$$\mathbf{S} = \begin{pmatrix} \sigma_x & \tau_{xy} & \tau_{xz} \\ \tau_{yx} & \sigma_y & \tau_{yz} \\ \tau_{zx} & \tau_{zy} & \sigma_z \end{pmatrix} \quad (1.4)$$

Since  $\tau_{xy} = \tau_{yx}$ ,  $\tau_{xz} = \tau_{zx}$ , and  $\tau_{yz} = \tau_{zy}$ , we need six independent values to describe the stress state of a point of a solid body. If the stresses are all parallel to one direction, the state of stress is uniaxial. In this case, the state of stress is considerably simplified because only the stress that coincides with the loading axis has a finite value while all the others are zero.

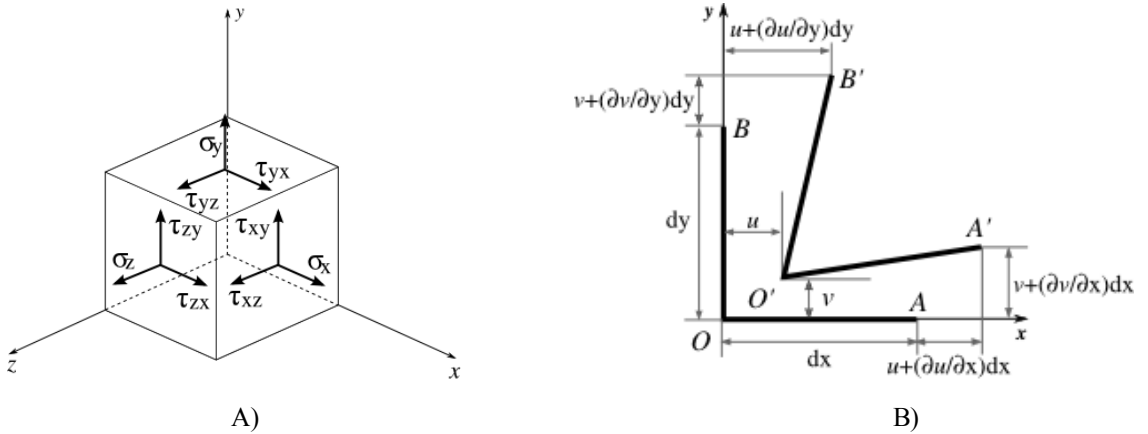


Figure 1.1 A) Stress components on an infinitesimal element, and B) Displacement of line elements .

## 1.2 ANALYSIS OF STRAIN

The displacement of any point in a body may be conveniently expressed in terms of its components  $u$ ,  $v$ ,  $w$  parallel to the  $x$ ,  $y$ ,  $z$  axes respectively. Consider two infinitesimal line elements  $OA$ ,  $OB$ , (Figure 1.1B) of lengths  $dx$ ,  $dy$  and parallel to the  $x$ ,  $y$  axes intersecting at the point  $O$ . Let these elements be displaced in the strained body into the positions  $O'A'$ ,  $O'B'$ . If we denote the displacements of the point  $O$  by  $u$ ,  $v$ , the corresponding displacements of  $A'$ ,

$B'$  are  $u + \frac{\partial u}{\partial x} dx$ ,  $v + \frac{\partial v}{\partial x} dx$  and  $u + \frac{\partial u}{\partial y} dy$ ,  $v + \frac{\partial v}{\partial y} dy$  respectively.

The normal strains [2] describe the change in length per unit length in each coordinate direction:

$$\epsilon_x = \frac{\partial u}{\partial x}, \quad \epsilon_y = \frac{\partial v}{\partial y}, \quad \epsilon_z = \frac{\partial w}{\partial z} \quad (1.5)$$

The shear strain [2] measures the decrease in the angle between two line segments initially orthogonal and parallel to the coordinate axes:

$$\gamma_{xy} = \frac{\partial v}{\partial x} + \frac{\partial u}{\partial y}, \quad \gamma_{yz} = \frac{\partial w}{\partial y} + \frac{\partial v}{\partial z}, \quad \gamma_{zx} = \frac{\partial u}{\partial z} + \frac{\partial w}{\partial x} \quad (1.6)$$

The subscripts have the same meaning as assigned for stresses.

### 1.2.1 Relations between stress and strain

If a homogeneous and isotropic body is subjected to an axial force (tension/compression), it experiments an axial (extension/contraction) strain in the direction of the force, that results in a transverse (contraction/expansion) strain in the two directions mutually perpendicular to the axial strain, Figure 1.2. While a material behaves elastically, there are a linear relationship between stress and strain given by Hooke's Law. Consider that the force is in the direction of the  $x$  axis, the longitudinal strain is given by:

$$\epsilon_x = \frac{\sigma_x}{E} \quad (1.7)$$

where  $E$  is the modulus of elasticity. As mentioned above the axial strain is accompanied by

simultaneous lateral strains, given by:

$$\epsilon_y = \epsilon_z = -\nu \epsilon_x \quad (1.8)$$

which  $\nu$  is a constant known as Poisson's ratio.

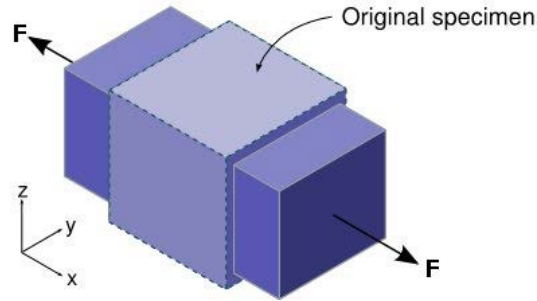


Figure 1.2 Deformation of a homogeneous, isotropic specimen under uniaxial load.

By measuring the displacement fields, stress and strain can be determined according to the above introduced equations.

### 1.3 STRESS-STRAIN DIAGRAM

In order to measure mechanical properties of a material various tests must be made to a sample. A universal testing machine, may be used to apply a tensile load, a compressive load or a deflection to a test specimen. From a tensile test properties as strength, stiffness, and ductility can be determined. A tensile test consists in apply a load using a computed controlled testing machine, the velocity must be uniform and controllable, and carefully selected since material properties are affected by high rates of loading. As the specimen is pulled the load is measured by the testing machine and recorded.

After the test a stress-strain diagram [3, 4], Figure 1.3, is constructed from the measurements taken during the test. The test starts at the origin *A*, the specimen starts to elongate with a linear relationship between stress and strain until point *B*, known as the *proportional limit*. After this point the specimen begins yielding, i.e., with a small or any increments of load an elongation is produced. The stress at point *C* is referred as the *yield point*. From *C* to *D* the

specimen continues to elongate without any increase in stress, The stress begins to increase at  $D$ , and the region from  $D$  to  $E$  is called zone of *strain hardening*. The stress at point  $E$  is referred to as *ultimate stress* or *ultimate strength*, this term is used to describe the maximum stress a material can withstand. At  $E$  the load begins to drop, and the specimen begins to neck down, this behavior continues until fracture occurs at the fracture stress  $F$ .

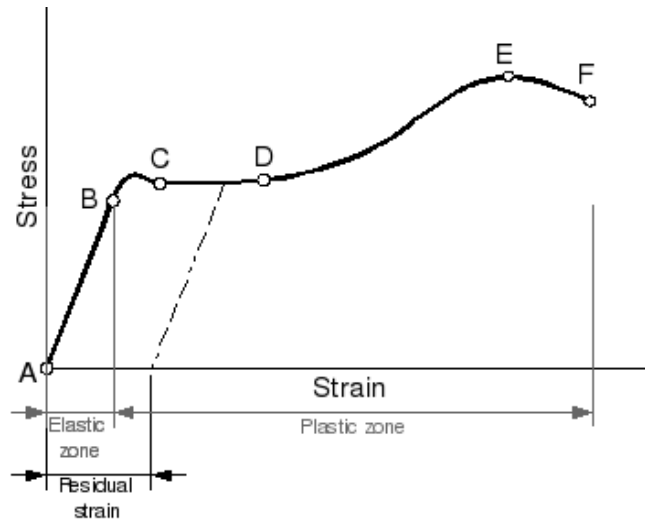


Figure 1.3 Stress-strain diagram.

From  $A$  to  $B$  the material is in the elastic zone, in this zone all deformations vanish when the load is removed. Between point  $B$  and  $C$  is the transition zone. Below point  $C$  begins the plastic zone, and when unloading from a point in this zone the stress-strain behavior of the specimen follows a straight line, Figure 1.3, whose slope is parallel to  $AB$ . The strain that remains when the stress return to zero is called residual strain.

Although the mechanical properties for materials as aluminum, hot-rolled steel and others are well defined, the importance to determine mechanical properties arise from that nowadays mechanical properties could be altered by different processes as alloying, work-hardening, and tempering, besides that a wide variety of new materials have been developed as plastics with improved properties, or composites. Composites are materials that combine two constituent materials in a manner that leads to improved mechanical properties, some of them are made by placing fibers in specific orientation to produce a material with direction-dependent properties.

## 1.4 STRESS CONCENTRATION

The average stress given by Equation 1.2 may be used only so long as the cross section of the members is relatively uniform, that is, there are no abrupt changes in cross section, because the stress will be uniformly distributed over the cross section, Figure 1.4.

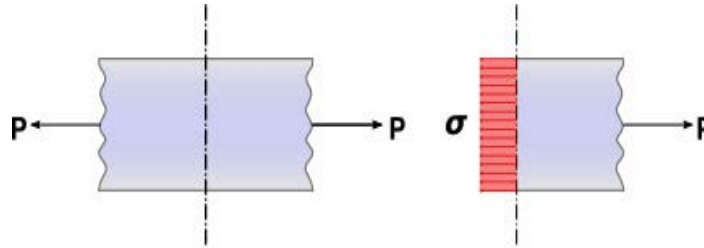


Figure 1.4 Stress distribution for a uniform cross section.

However, if there are abrupt changes in cross section, the stress distribution will no longer be uniform. Consider a cracked plate subjected to a tensile stress. Since the tensile stress cannot be transmitted through the crack, the load must be redistributed over the remaining material in an uneven pattern that is highest at the edges. The lines of force are diverted around the crack resulting in a local stress concentration. In the infinite plate, Figure 1.5A, the line of force at a distance  $W$  from the crack center line has force components in the  $x$  and  $y$  directions, figure. If the plate is restricted to  $2W$ , Figure 1.5B, the force  $x$  must be zero on the free edge, this boundary condition causes the lines of force to be compressed which results in a higher stress intensification at the crack tip [5]. The maximum stress could be higher than the average stress given by Equation 1.2.

Depending of the material used and the loads of which will be subjected, this stress concentrations may or may not be significant for the design. Although the exact distribution of stress is not of great importance, the maximum value of stress if it is. This maximum stress may be related to the average stress on the net cross section, by the stress concentration factor  $K$ :

$$\sigma_{max} = K \sigma \quad (1.9)$$

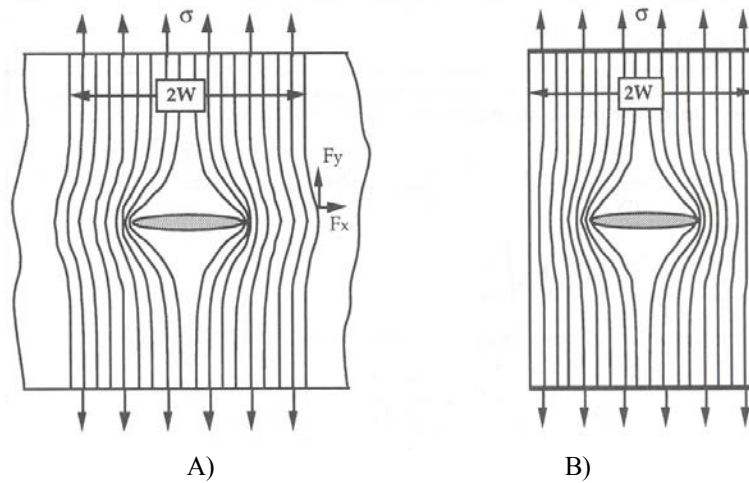


Figure 1.5 Stress concentration effects due to a crack in: A) infinite and B) finite width plate.

The stress concentration factor can be determined both theoretically and experimentally, it depends on the geometry and dimensions of the cross section changes and the type of load applied (axial loading, torsion or bending). Figure 1.6 shows an example of the stress concentration factor for a hole in a rectangular bar. It is important to notice that a very small hole can have a very damaging effect on a member. Values of stress concentration are based on linearly elastic behavior and are valid only as long as the computed value  $\sigma_{max}$  does not exceed the proportional limit of the material.

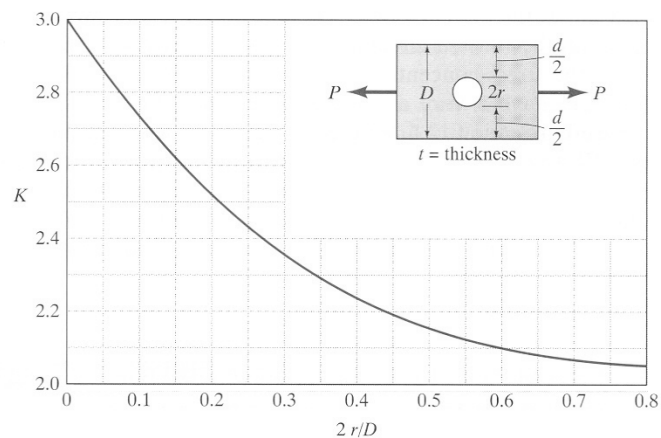


Figure 1.6 Stress concentration factor  $K$  for a flat bar with centrally located hole in tension.

A ductile material, due to its high elongation after yield, has the quality of redistributing stress

in areas of high concentration of stress. Consider a bar with a hole, Figure 1.7A, where abrupt changes occur in the area of the cross section of a member, as half of the hole, the stress are not evenly distributed. The maximum normal stress occurs at the edges of the hole on the cross section which passes through the center of the hole, Figure 1.7B. If the material is ductile, the fibers near to the hole stress until the yield point. These fibers are deformed but maintain this stress. The excess of stress would have to be applied to these fibers is supported by adjacent fibers, Figure 1.7C. If some fibers stress until the elastic limit of the material, do not break, instead of that, support the load and the strain continue until all fibers reach the yield point, resulting in a stress redistribution, Figure 1.7D. If some fibers fracture, the fracture of some fibers in the cross section reduce the area and consequently more fibers are overloaded to the high intensity. Finally these fibers break and as the process continue develops a progressive crack. A small crack develops quickly causing that the entire member fracture [4].

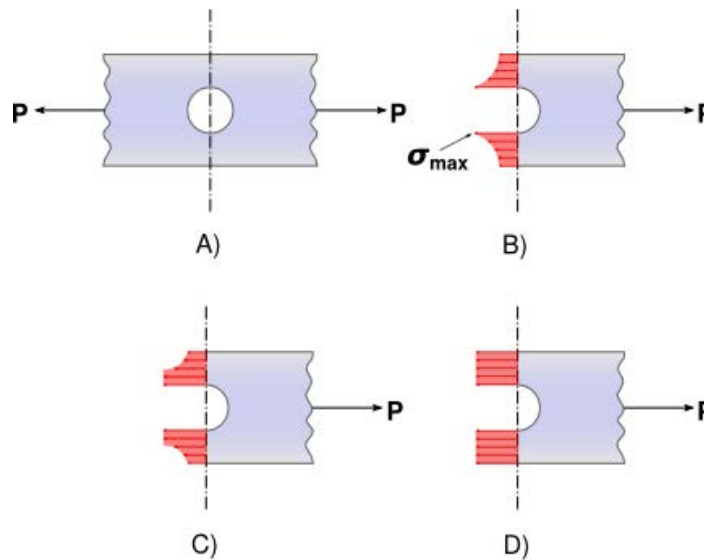


Figure 1.7 Stress distribution in a nonuniform cross section. A) Non uniform cross section, B) Stress distribution below the yield point, C) Maximum stress over yield point, and D) All fibers at the yield point.

From the fracture mechanics approach, fracture cannot occur unless the stress exceeds the ultimate strength of the material. Thus the flaws (hole, notch, etc.) must lower the global strength by magnifying the stress locally. Loading produces a singularity at the crack tip, that is, a region with a determined distribution of stress fields. The stress concentration factor defines the amplitude of the crack tip singularity, that is, stresses near the crack tip increase in



proportion to the stress concentration factor, and stresses far from the crack tip are governed by remote boundary conditions.

A plastic zone forms ahead of the crack tip, as this region grows the elastic stress analysis become increasingly inaccurate. Simple corrections to linear elastic fracture mechanics are available when moderated crack tip yielding occurs. For more extensive yielding, one must apply alternative crack tip parameters that take nonlinear material behavior into account [5].

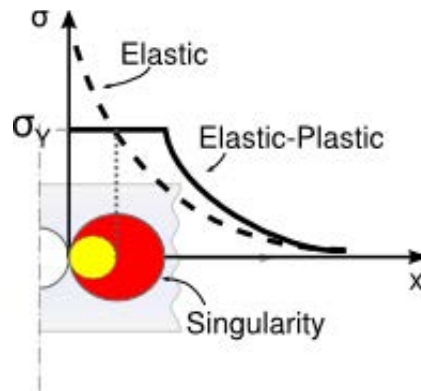


Figure 1.8 The small circle represents load that must be redistributed, resulting in a larger plastic zone.

The stress singularity is truncated by yielding at the crack tip, in the elastic crack tip solution. When yielding occurs, stresses must redistribute in order to satisfy equilibrium. The small circle in Figure 1.8 represents a region in which are forces that would be present in an elastic material but cannot be carried in the elastic-plastic material because the stress cannot exceed yield, this loads must be redistributed. The plastic zone must increase in size in order to accommodate these forces.

## REFERENCES

1. Kreis T., *Holographic Interferometry: Principles and Methods*, Chapter 5, Akademie Verlag, Bremen (1996)
2. Kuske A., Robertson G., *Photoelastic Stress Analysis*, Chapters 1 and 2, Wiley, Chichester

(1974)

3. Craig R.R., *Mechanics of Materials*, Chapters 2 and 12, Wiley, New York (1999)
4. Fitzgerald R.W. *Mecánica de Materiales*, Chapters 2, 10 and 12, Alfaomega, Bogotá (2002)
5. Anderson T.L., *Fracture Mechanics: Fundamentals and Applications*, Chapters 1 and 2, CRC Press LLC, Boca Raton (1995)

## CHAPTER 2

### MOIRÉ AND FRINGE PROJECTION TECHNIQUES

---

The term moiré against what might be thought is not a name of a person, in fact, it is a french word referring to a silk fabric that produces dark bands [1]. In optics is used to describe a common effect that is observed when two identical or closely identical amplitude gratings are superimposed, this effect could be seen in our everyday surroundings with ordinary objects. The gratings can be of straight lines or curves, when two gratings overlap, some of the light passing through the first grating is obstructed by the second one, and a modulation of the light intensities take place, producing a pattern of much lower frequency, known as moiré fringes. A dark fringe is produced where the dark lines are out of step one-half period, and a bright fringe is produced where the dark lines for one grating fall on top of the corresponding dark lines for the second grating [2]. The phenomenon is dependent to the observer direction of view.

Moiré effect is related to interferometry, and help us to understand interferometric test results. A grating can be thought as a plane wave where the distance between two lines is equal to the wavelength of light, then the superposition of two gratings is equivalent to the superposition of two wavefronts. A circular grating represents a spherical wavefront. Where the two waves are in phase, bright fringes result (constructive interference), and where they are out of phase, dark fringes result (destructive interference). The moiré pattern obtained from superimpose two gratings (linear or circular) is equivalent to the interference pattern resulting from superimpose two wavefronts (plane or spherical).

Moiré is one of the first optical methods used to measure displacements. There are moiré techniques for measure in-plane and out-of-plane components of displacements, the displacements are measured simultaneously over the whole field of view, without contact. The main principle of moiré technique is to compare two states of the same system of lines, that reflect the changes experimented by a surface. There are three basic types of moiré:

- Intrinsic moiré gives information concerning displacements taking place on a surface.

- Projection or shadow moiré provides displacements of a surface with respect to a reference plane.
- Reflection moiré provides information about the slopes of a surface.

A theoretical description of moiré fringes formation is given in Section 2.1. The methods to measure in-plane deformations and strains are briefly described in Section 2.2. Moiré techniques for out-of-plane deformations, contouring and fringe projection are described in Section 2.3.

## 2.1 MATHEMATICAL DESCRIPTION

Due to the gratings are periodic structures their intensity transmission function could be described using Fourier series, then the transmittance of the two gratings can be given by:

$$T_1(x, y) = a_0 + \sum_{m=1}^{\infty} a_m \cos[m \phi_1(x, y)] \quad (2.1)$$

$$T_2(x, y) = b_0 + \sum_{n=1}^{\infty} b_n \cos[n \phi_2(x, y)] \quad (2.2)$$

where  $a_0$ ,  $a_m$ ,  $b_0$  and  $b_n$  are the Fourier coefficients that determine the profile of the grating lines (i.e., square wave, triangular, sinusoidal, etc.), and  $\phi(x, y)$  is the function describing the basic shape of the grating lines. Assuming that two gratings are oriented with an angle

$2\theta$  between them with the y axis bisecting this angle, Figure 2.1, the two grating functions can be written as:

$$\begin{aligned} \phi_1(x, y) &= \frac{2\pi}{p_1} ([x - f_1(x, y) - \delta_1] \cos \theta + y \sin \theta) \\ \phi_2(x, y) &= \frac{2\pi}{p_2} ([x - f_2(x, y) - \delta_2] \cos \theta - y \sin \theta) \end{aligned} \quad (2.3)$$

where  $p$ ,  $f$  and  $\delta$  are the grating periods, the local deformations of the grating lines and the in-plane grating displacement, respectively. The function  $f_1(x, y)$  represents the departure of grating lines from straightness. In strain analysis is the in-plane deformation of the object under load, in moiré topography it is the out-of-plane deformation [3].

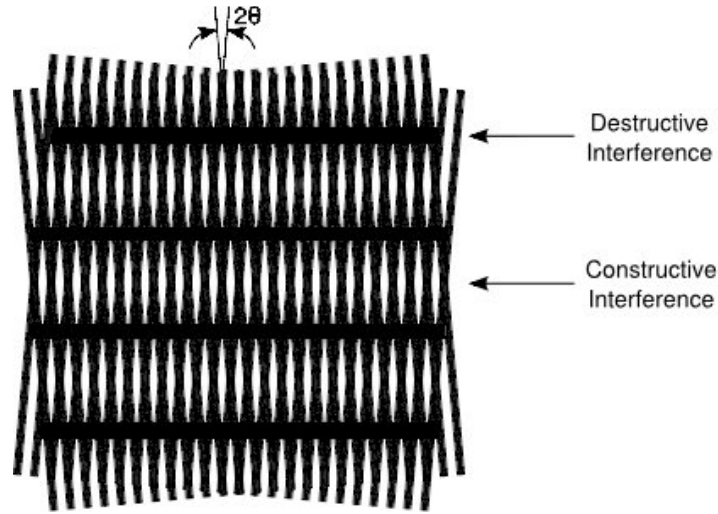


Figure 2.1 Moiré pattern between two overlap gratings of the same pitch at an angle  $\theta$ .

To make it possible to form moiré fringes of good visibility the following conditions should be fulfilled:

- The widths of the lines and spaces are equal.
- The two gratings are well defined, i.e.,  $f_1(x, y)$  and  $f_2(x, y)$  are smoothly varying functions.
- The angle of intersection of the two gratings should be small. If the angle between gratings is increased the separation of moiré fringes decreases.
- The ratio of the grating periods should be in the integer ratio,  $d_1 \approx M d_2$ .

When the gratings are superimposed, the resultant transmission is given by the product:

$$T_1(x, y)T_2(x, y) = a_0 b_0 + a_0 \sum_{n=1}^{\infty} b_n \cos[n\phi_2(x, y)] + b_0 \sum_{m=1}^{\infty} a_m \cos[m\phi_1(x, y)] + \sum_{n=1}^{\infty} \sum_{m=1}^{\infty} a_m b_n \cos[m\phi_1(x, y)] \cos[n\phi_2(x, y)] \quad (2.4)$$

The first three terms on Equation 2.4 represent the original gratings, the last term is the interesting one, and can be rewritten as:

$$Term\ 4 = \sum_{n=1}^{\infty} \sum_{m=1}^{\infty} \frac{a_m b_n}{2} [\cos[m\phi_1(x, y) + n\phi_2(x, y)] + \cos[m\phi_1(x, y) - n\phi_2(x, y)]] \quad (2.5)$$

We are interested in the lowest beat frequency term that determine the moiré fringes, then

ignoring high frequency terms the general moiré fringe formula can be written as:

$$T_M(x, y) = a_0 b_0 + \sum_{n=1}^{\infty} \sum_{m=1}^{\infty} \frac{a_m b_n}{2} \cos[m \phi_1(x, y) - n \phi_2(x, y)] \quad (2.6)$$

from which can be deduced the fringe spacing, orientation and the fringe profile. The moiré will be lines whose centers satisfy the equation:

$$\phi_1(x, y) - \phi_2(x, y) = 2\pi r$$

or using Equations 2.3:

$$\frac{1}{p_1} ([x - f_1(x, y) - \delta_1] \cos \theta + y \sin \theta) - \frac{1}{p_2} ([x - f_2(x, y) - \delta_2] \cos \theta - y \sin \theta) = r \quad (2.7)$$

where  $r$  is an integer corresponding to the fringe order.

Three special cases can be analyzed [2], considering straight lines,  $f_1 = f_2 = 0$ , without in-plane displacements  $\delta_1 = \delta_2 = 0$ .

Case 1: Pure rotation. Where equal gratings are superimposed with an angle between them,  $p_1 = p_2 = p$  and  $\theta \neq 0$ .

Equation 2.7 is reduced to:

$$2y \sin \theta = rp \quad (2.8)$$

This equation represent equally spaced, horizontal lines.

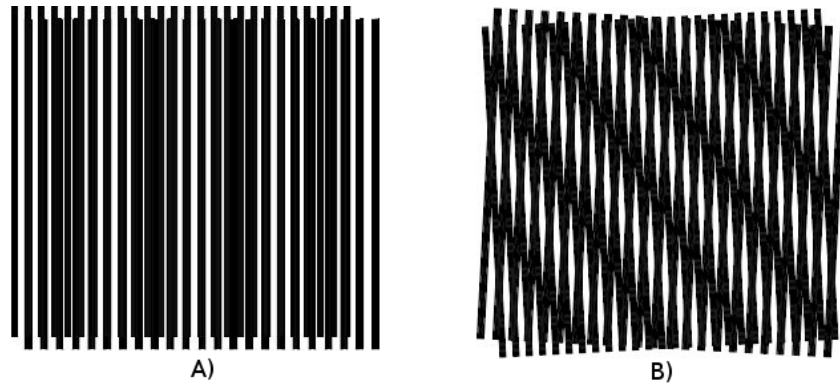


Figure 2.2 Moiré patterns formed by: A) Two gratings of different pitches and no tilt, B) Two gratings of different pitches and tilted.

Case 2: Pure extension. Gratings of slightly different periods are superimposed parallel to each other,  $p_1 \neq p_2$  and  $\theta = 0$ .

The moiré fringes satisfy the equation:

$$x = \frac{p_1 p_2}{p_2 - p_1} r \quad (2.9)$$

This fringes are equi-spaced, vertical lines, Figure 2.2A.

Case 3: General case. Where the two gratings have different line spacings and the angle between the gratings is nonzero:

$$x \left( \frac{1}{p_1} - \frac{\cos \theta}{p_2} \right) + y \frac{\sin \theta}{p_2} = r \quad (2.10)$$

This is the equation of straight lines whose spacing and orientation is dependent on the relative difference between the two grating spacings and the angle between the gratings, Figure 2.2B.

## 2.2 IN-PLANE DIPLACEMENTS

Consider a point P on the surface of a solid body that displaces to a point P', Figure 2.3, by a deformation or by rigid-body movement, or by a combination of both. The displacement of P is represented by vector  $\vec{d}$  and its components  $\hat{i}$ ,  $\hat{j}$ ,  $\hat{k}$  in the  $x$ ,  $y$ ,  $z$  directions respectively. The displacement is described by scalars  $u$ ,  $v$ ,  $w$  which are the magnitudes of the corresponding vectors.

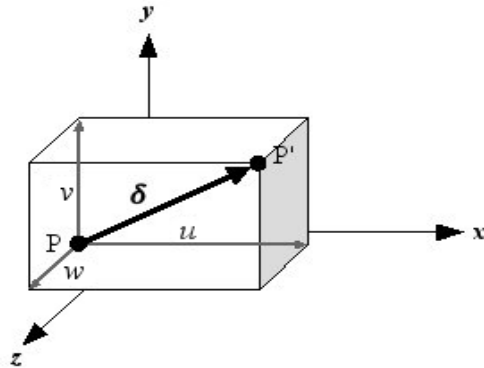


Figure 2.3 A three-dimensional displacement.

$u$  and  $v$  are in-plane displacements since  $u$  and  $v$  lie in the original plane of the surface,  $w$  is perpendicular to the surface and it is called the out-of-plane displacement. In-plane

displacements can be measure independently by geometric moiré and moiré interferometry [4, 5]. To measure in-plane deformations a grating is attached to the test surface, and a reference grating is fixed to the surface, when the surface is deformed or experiences a body rigid translation the specimen grating will follow the deformation and the moiré pattern appear.

There are several methods to obtain the moiré pattern, the main difference is that in some of them the intensities are added, and in other are multiplied. For the additive type the moiré pattern could be obtained by: (1) double exposure, first imaging the reference grating and after deformation imaging the specimen grating onto the same film, (2) imaging the reference grating onto the specimen grating by forming the reference grating by means of interference between two plane waves. For the multiplicative type the moiré pattern could be obtained by: (1) placing the reference grating in contact with the specimen grating, (2) imaging the specimen grating and placing the reference grating in the image plane, scaled according to the image magnification, (3) imaging the reference grating onto a photographic film and thereafter image the specimen grating after deformation onto another film, then the two films are laid in contact.

As the frequency of the fringes increase the contrast is reduced, when high frequency gratings are used the direct observation of moiré fringes is impossible. The observation of the moiré effect with incoherent light depends on the diffraction effect caused by the gratings used. Somewhere between *40 and 50 lines per mm*, the moiré fringe modulation becomes very low, due to dispersion of the different wavelengths of the white light. For frequencies higher than *50 lines per mm*, coherent illumination must be used for the observation of moiré patterns in the first diffracted orders, this is the case of moiré interferometry. The difference between using incoherent or coherent illumination is that with incoherent light intensities are added, and in the other case, light vectors are added with their respective phases [1].

Where strains are required, they can be extracted from the displacements fields.



## **2.3 OUT-OF-PLANE DISPLACEMENTS**

Moiré techniques are useful to contour surfaces that are too coarse to be measured with standard interferometry. Some of the advantages that this techniques offer are that the data acquisition is fast so the analysis can be done in real-time, and the resolution may be varied. There are three techniques: (1) shadow moiré, (2) projection moiré, and (3) reflection moiré. The first two are for objects which reflect light diffusely, and the last one is used for objects which give specular reflection. Another technique for obtain out-of-plane displacements is the so called fringe projection, though this technique does not use the moiré effect has a lot of similitude with projection moiré. Each of this techniques will be briefly described in this section.

### **2.3.1 Shadow moiré**

Some of the first authors who gave a theoretical description and reported the use of shadow moiré to measure the surface topography were Takasaki [6] and Meadows [7]. This technique consists on place a linear amplitude grating, usually of binary or sinusoidal transmittance, over an object under study. A method to use a computer generated grating (CGG) was developed for Asundi [8], of course, the grating has to be created on a transparent display. A liquid crystal display (LCD) projection panel could be used for this purpose, but become necessary to use normal view because the low contrast of these panels. The advantage of use CGG is that the period of the grating could be changed rapidly and thus instantaneously view the resultant moiré fringes.

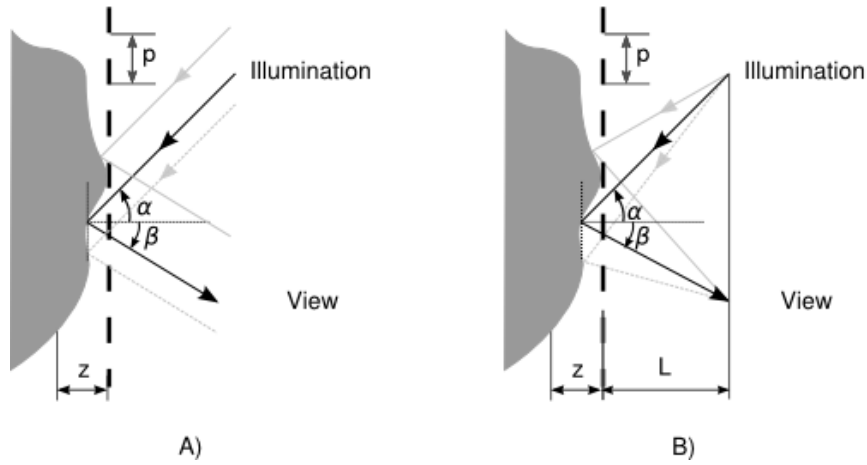


Figure 2.4 Geometry of shadow moiré with: A) illumination and viewing at infinity, B) illumination and viewing at finite distances.

Assuming that the grating is obliquely illuminated with collimated light under an angle of incidence  $\alpha$ , and the light that is scattered by the specimen is viewed at infinity under an angle  $\beta$ , both measured from the grating normal, Figure 2.4A. The specimen surface should be prepared with a matte white paint in order to scatter enough light. The source do not need to be coherent. The grating is coarse enough so that diffraction effects can be ignored, however, the grating should be close enough to the object surface, when surface height variations are large compared to the grating period diffraction effects will occur, by these reason maximum contrast of fringes is achieved for almost flat surfaces.

The shadow of the grating casts on the object surface. The moiré pattern is observed between the shadow and the grating lines. the height  $z$  between the object and the grating can be determined from Figure 2.4, and is given by:

$$z = \frac{Np}{\tan \alpha + \tan \beta} \quad (2.11)$$

where  $p$  is the period of the grating,  $N$  is a number of grating lines between the point A and B ( $N$  is fringe number is expressed by  $N = \frac{\phi}{2\pi}$ ). The contour interval in a direction perpendicular to the grating is given by:

$$C = \frac{p}{\tan \alpha + \tan \beta} \quad (2.12)$$

The contour interval decreases as the angle between observation and illumination increases.

When plane wave illumination and observation from infinity is used the sensitivity is constant, unfortunately large surfaces are impossible to cover with plane waves. Therefore it is possible to derive the case of finite illumination and viewing distance from the general case. If a point source is used to illuminate the object surface, and the viewing point is at a finite distance, the sensitivity is not constant and depends on position of each point, Figure 2.4B, but when the illumination source and observation are placed at a same distance  $L$  from the plane of the grating and  $L \gg z$ , even the angles vary point to point on the surface, the sum of their tangents remains constant, hence the sensitivity will be constant and the contour interval will be the same as that given by Equation 2.12.

Because of the finite distances there is also distortion due to viewing perspective. A point  $P$  on the surface will be apparently at  $P'$  when viewed through the grating. By simple geometry the actual coordinates  $(x,y)$  could be obtained from the measured coordinates  $(x',y')$ :

$$x = x' \left( 1 + \frac{z}{L} \right), \quad y = y' \left( 1 + \frac{z}{L} \right) \quad (2.13)$$

this enables the measured surface to be mapped to the actual surface to correct for the viewing perspective.

The moiré pattern formed is crossed by the lines of the grating, this lines can be smeared out by a few different methods [3, 4]. One method consist on translating the grating during the time interval of the photographic exposure, the moiré fringes remain stationary because the grating and it shadow are subject to identical phase change and the grating lines are averaged making them invisible, this could be achieved too averaging video frames during the translation of the grating. Another method for gratings with lines and spaces of equal widths consists in use double exposure, translating the grating half period between exposures. Other possibility is not to resolve the grating lines, while the coarser moiré fringes remain resolved. The elimination of the grating lines become necessary for fringe processing.

Shadow moiré has several industrial applications but not as many as it could be supposed. This

method has the disadvantage of offer lower measurement sensitivity than the accuracy obtained by mechanical 3D measuring machines. Patorski [3] gives a lot of references of applications. Some of the applications that worth mention are:

- Strength of components.
- Deformation tests.
- Studies of vibrations.
- Contouring.
- Human body measurement.

### 2.3.2 Projection moiré

Projection moiré technique [9-12] consists on project fringes onto the surface under test and then viewing through a second grating in front the viewer. The fringes can be projected on a surface by means of interference between two coherent waves formed in a interferometer or by imaging a grating using a projection system, Figure 2.5. The grating used can be CGG or physical, if phase shifting is required, to use a CGG has the advantage of effect easily the shift via software instead than mechanically [8].

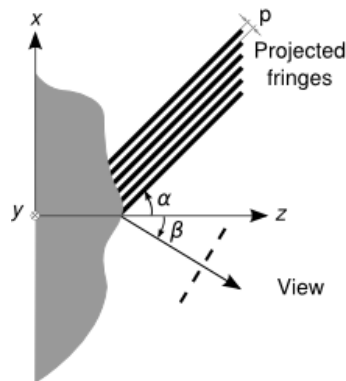


Figure 2.5 Geometry of projection moiré.

Assuming collimated illumination and viewing at infinity the mathematical description is the same as that for shadow moiré. The difference between projection and shadow moiré is that two different gratings could be used in the first one. The contour interval is given by Equation 2.12, when both gratings have the same pitch  $d$ . This is not always the case, a wide theoretical review of the projection technique is given by Benoit *et al.* [12].

The moiré pattern could be obtained using different methods: (1) taking a photograph of the object in its initial state, after some change of the object another photograph is taken, then two films are superimposed, (2) using a reference grating in the image plane of the observation system, (3) recording the object on its original state to use it as a reference grating, after some change the fringes will change and a second image is recorded, the moiré fringes appear from the interaction of this image and the reference grating [13], (4) using two projection systems [3, 4] from symmetrical angles with respect to the normal of the reference plane, lines of individual gratings must be resolved by the camera in order to record moiré fringes.

The first method is useful for detect changes of shape only, contouring can not be achieved since it is impossible to superimpose images that are recorded before and after the change [3]. The moiré fringes obtained by the second method are a contour map of the object respect to a plane, but grating lines must be resolved. When the third method is used, it is possible to obtain the out-of-plane deformation of an object, or a contour map if a plane surface is used as the object in the first exposure.

The grating lines reduce the fringe visibility of the resultant moiré pattern, as in shadow moiré the grating lines can be eliminated with moving gratings [14].

Projection moiré has the advantage to contour objects much larger than with shadow moiré, and the fringe patterns are much easier to process. Some of the applications [11, 15-19] are:

- Measurement of strains.
- Selection of components comparing them with a master.
- Automation of technological processes.
- Vibration analysis.
- Human engineering.

### **2.3.3 Fringe projection**

Fringe projection is a technique based on projection moiré. The operating principle can be described as follows. A fringe pattern is projected onto the surface under test, and the

deformed fringe pattern is viewed from another direction by a camera, it is a common practice to set the viewing axis normal to the  $x$ - $y$  plane. The main difference between both techniques is that in fringe projection a reference object or plane can be evaluated first and the results of the test object subtracted from this to give the desired contours.

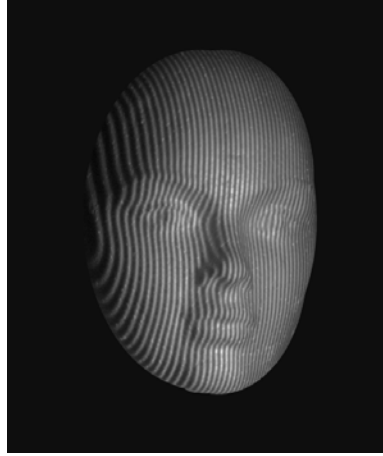


Figure 2.6 Projected fringes on an object

For the case of collimated illumination and viewing at infinity, straight equally spaced fringes are incident on the object, producing equally spaced contour intervals [2]. The viewer observes fringes over the object surface, Figure 2.6, the departure of a viewed line from the straightness shows the departure of the surface from a plane reference surface. When the projected fringes with period  $p$  are viewed at an angle  $\alpha$  have a spacing  $d$  perpendicular to the viewing direction given by:

$$d = \frac{p}{\cos \alpha} \quad (2.14)$$

Assuming normal view, the height of the object above the reference plane will be:

$$z = \frac{\phi}{2\pi} \frac{p}{\sin \alpha} = \frac{\phi}{2\pi} \frac{d}{\tan \alpha} \quad (2.15)$$

As the angle between illumination and observation become larger the contour interval decreases, even though a large angle gives high sensitivity, either could produce unwanted shadows on the object, these shadows represent areas with missing data where the object cannot be contoured.

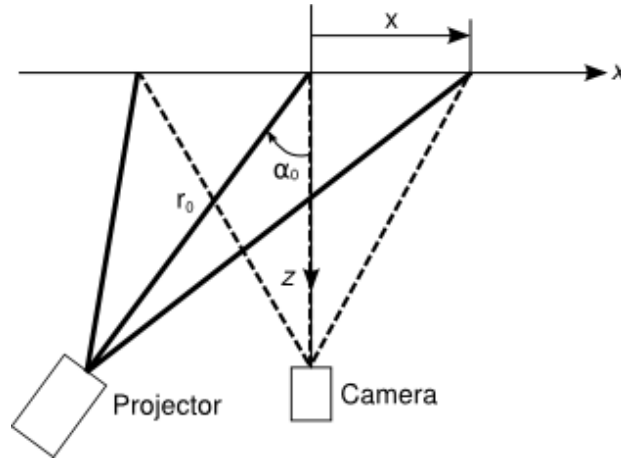


Figure 2.7 Geometry of fringe projection with uncollimated light

For large objects it is not possible to use collimated illumination, thus the period  $d$  will vary with the  $x$  coordinate, Figure 2.7, the height will be a function of the distance from the source and viewer to the object, a good approximation has been derived by Gasvik [13], assuming normal view:

$$z = \frac{\phi}{2\pi \sin \alpha_0} \frac{d_0}{r_0} \sqrt{\left(\sin \alpha_0 + \frac{x}{r_0}\right)^2 + \cos^2 \alpha_0} \quad (2.16)$$

where  $d_0$  is the value of the period  $p$  at the origin,  $\alpha_0$  is the angle between the optical axis of the projection system and the  $z$  axis and  $r_0$  is the distance from the image point of the light source to the origin,  $x$  is the distance along the object measured from the origin which is usually the center of the object. There will be distortion due to perspective, the same correction factors given for shadow moiré in Equation 2.13 can be applied.

#### 2.3.4 Reflection moiré

Reflection moiré [3, 19] method uses the superimposition of two grating images formed by a beam reflected from the surface under test. The smoothness of the surface  $S$  makes it possible to image the mirror image of the grating  $G$  by means of the lens  $L$ , Figure 2.8. The first image corresponds to the surface in its reference state. The second image gives the variation of the surface from the reference state.

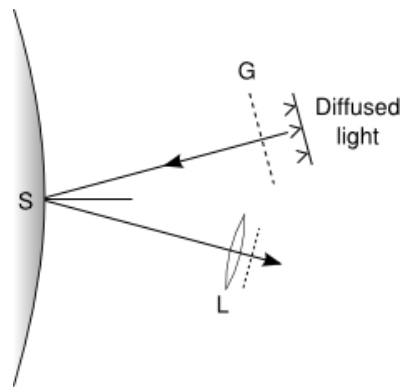


Figure 2.8 Reflection moiré

The moiré can be produced as in previous methods: (1) by placing a grating in the image plane of  $L$ , or (2) by double exposure, photographing the mirror image of  $G$  before and after deformation of  $S$ . The result gives the slopes and curvatures at all points of the surface, i.e. the first and second derivatives of the out-of-plane displacement. This method can be applied on shiny mirror-like surfaces and phase-objects.

## REFERENCES

1. Sciammarella C. A., "Moiré in Science and Engineering", *Trends in Optical Nondestructive Testing and Inspection*, Rastogi P. and Inaudi D., Editors, Elsevier, Amsterdam (2000)
2. Creath K., Wyant J. C., "Moiré and Fringe Projection Techniques", *Optical Shop Testing*, Malacara D., Editor, Wiley, New York (1992)
3. Patorski K., *Handbook of the Moiré Fringe Technique*, Chapters 1, 9-11, Elsevier, Amsterdam (1993)
4. Post D., Han B., Ifju P., *High Sensitivity Moiré: Experimental Analysis for Mechanics and Materials*, Chapters 3 and 4, Springer, New York (1994)
5. Martínez Amalia, Rodríguez-Vera R., Rayas J.A., "Fracture Detection by Grating Moiré and In-Plane ESPI Techniques", *Opt. Lasers Eng.*, **39**, pp. 525-536 (2003)
6. Takasaki H., "Moiré topography", *Appl. Opt.*, **9**, pp. 1467-1472 (1970)
7. Meadows D. M., Johnson O., Allen J. B., "Generation of Surface Contours by Moiré Patterns", *Appl. Opt.*, **9**, pp. 942-947 (1970)



8. Asundi A., "Digital Moiré for Deformation Analysis", *Trends in Optical Nondestructive Testing and Inspection*, Rastogi P. and Inaudi D., Editors, Elsevier, Amsterdam (2000)
9. Brooks R. E., Heflinger L. O., "Moiré Gauging Using Optical Interference Patterns", *Appl. Opt.*, **8**, pp. 935-939 (1969)
10. MacGovern A. J., "Projected Fringes and Holography", *Appl. Opt.*, **11**, pp. 2972-2974 (1972)
11. Gasvik K. J., "Moiré Technique by Means of Digital Image Processing", *Appl. Opt.*, **22**, pp. 3543-3548 (1983).
12. Benoit P., Mathieu E., Hormière J., "Characterization and Control of Three-Dimensional Objects Using Fringe Projection Techniques", *Nouv. Rev. Opt.*, **6**, pp. 67-86 (1975)
13. Gasvik K. J., Fourny M. E., "Projection Moiré Using Digital Video Processing: A Technique for Improving the Accuracy and Sensitivity", *Transactions of the ASME*, **53**, pp. 652-656 (1986)
14. Halioua M., Krishnamurthy R. S., Liu H., "Projection Moiré With Moving Gratings for Automated 3-D Topography", *Appl. Opt.*, **22**, pp. 850-855 (1983)
15. Der Hovanesian J., Hung Y. Y., "Moiré Contour-Sum Contour-Difference, and Vibration Analysis of Arbitrary Objects", *Appl. Opt.*, **10**, pp. 2734-2738 (1971)
16. Rowe S. H., "Projected Interference Fringes in Holographic Interferometry", *J. Opt. Soc. Am.*, **61**, pp. 1599-1603 (1971)
17. Doty J.L., "Projection Moiré for Remote Contour Analysis", *J. Opt. Soc. Am.*, **73**, pp. 366-372 (1983)
18. Michalski M., Rabal H. J., Garavaglia M. J., "Operations Using Fringe Projection", *Appl. Opt.*, **25**, pp. 4338-4342 (1986)
19. Gasvik K. J., *Optical Metrology*, Chapter 7, Wiley, England (2002)

## CHAPTER 3

### PHASE MEASUREMENT

---

For many years, the analysis of interferograms was done manually, with the use of computers the analysis of interferograms become simple. The main advantages of digital image processing are: better accuracy, increase the speed, and automation of the process.

Fringe analysis can be done from a single image or from multiple images. Fringe analysis methods can be divided in two classes: (1) those that first reduce the image to a list of digitized fringe centers and (2) those that directly process the entire fringe to obtain the measured phase [1]. Fringe analysis from multiple images is more accurate but has the limitation of that air turbulence and mechanical conditions should remain constant over the time required to obtain the images, when these requirements are not fulfilled, we can analyze just one interferogram, because the image could be acquired over a brief time interval, but at the cost of have less precision.

The first case refers to intensity-based techniques, and before the development of phase-measurement techniques, second case, they were the only tools available for interferogram analysis. These techniques basically consist of two steps: locating the fringe centers, either manually or with the computer, and assigning fringe order numbers. The fringe centers represent discrete measurement points and some data interpolation is necessary to generate a square grid of data that represent a map of the optical path difference. There are three main problems associated with these techniques: (1) the accuracy of the measured positions of the fringe centers is often less than desired, (2) not enough data points are obtained in most cases, to increase the density of data points, more fringes could be generated, but then, the accuracy is reduced because of the mistakes to locate fringe centers, (3) the interpolation process to obtain a square grid of data can introduce error into the results.

Phase-measurement technique most widely used is phase-measurement interferometry (PMI)

and can be divided in two main categories: temporal and spatial. Temporal PMI are those which take the phase data sequentially, as phase shifting, and spatial PMI are those which take the phase data simultaneously, as multichannel interferometers [2-4], spatial synchronous detection [5] and Fourier transform method (FTM) [6].

On the other hand techniques for determining phase can be split into two basic categories: electronic and analytical. For electronic techniques, hardware is used to monitor interferogram intensity data as the phase is modulated [7]. The phase is encoded in the variations in the intensity pattern of the recorded interferograms and a simple point-by-point calculation recover the phase [5]. Some electronic techniques are heterodyne interferometry [8-11], phase lock or AC interferometry [12-15], and zero crossing techniques [8, 13]. For analytical techniques, intensity data are recorded while the phase is temporally modulated, sent to a computer and then used to compute the relative intensity measurements [7]. Analytical techniques use phase-shifting or the FTM, although many authors consider FTM as a fringe analysis technique instead of a phase-measurement technique. The phase obtained using any of the above techniques is in modulo  $2\pi$ , and is necessary to remove these discontinuities to obtain the final phase map.

Developments and cost reduction in solid-state-detector arrays and fast computers have favored the use of analytical techniques. When a solid-state-detector array is used for acquire the image of the interferogram, this image is stored as an array of picture elements (pixels), with each pixel represented as a numerical value corresponding to the image gray level at that location, this data are sent to a computer making possible measure the phase at every position simultaneously, eliminating the need of scan or use a large number or redundant circuits as in the past [7].

In this chapter analytical techniques will be described. In Section 3.1 phase-shifting technique is described, in Section 3.2 we describe FTM is described, and finally in Section 3.3 phase unwrapping is treated.

### 3.1 PHASE SHIFTING

The main principle of phase shifting technique is that a suitable system shifts the phase by a known amount between measurements to produce a time-varying signal at each point in the fringe pattern. There are two types of phase shifting techniques: (1) those that integrate the intensity while the phase is being increased linearly, referred to as integrating-bucket technique [5], Figure 3.1A, and (2) those that step the phase a known amount between intensity measurements, known as phase-stepping technique [5], Figure 3.1B. The phase stepping method is briefly described below.

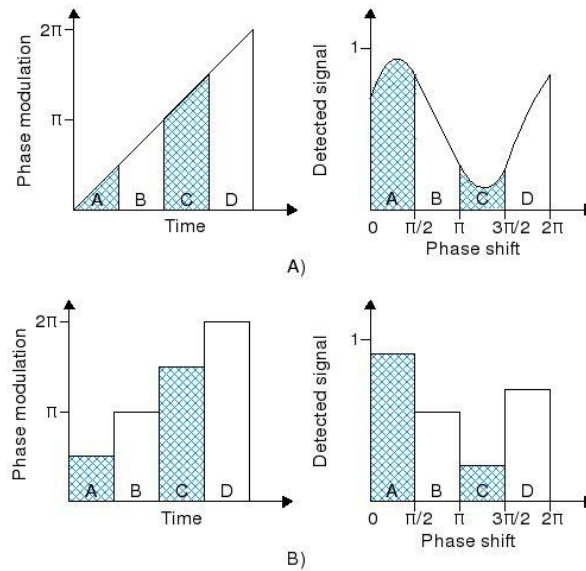


Figure 3.1 Phase modulation and detected signal for: A) integrating-bucket, and B) phase-stepping.

Some advantages of phase-shifting are: any type of fringe pattern can be analyzed including closed fringes, unambiguously determination of the sense of the part (concave or convex), is insensitive to spatial variations of intensity, detector sensitivity, and fixed pattern noise.

The phase shift could be induced with various methods, like using a piezoelectric, moving a grating, translating a mirror, tilting a glass plate, or rotating a half-wave plate or analyzer, to mention a few [5, 7].

The intensity of a fringe pattern is given by:

$$I(x, y) = a(x, y) + b(x, y) \cos(\phi(x, y) + \alpha) \quad (3.1)$$

where  $a(x, y)$  describes the background intensity variations in the fringe pattern,  $b(x, y)$  describes the amplitude of fringes,  $\phi(x, y)$  is the required phase information and  $\alpha$  is the introduced phase shift. Equation 3.1 contains three unknowns  $a$ ,  $b$ , and  $\phi$ , so at least three intensity measurements are required to determine the phase.

Several algorithms have been developed, all of them share common characteristics:

- A series of interferograms must be recorded as the reference phase is varied.
- The phase modulo  $2\pi$  is then calculated at each measurement point as the arctangent of a function of the interferogram intensities measured at that individual point.
- The final phase map is then obtained by unwrapping the phase to remove the  $2\pi$  discontinuities.

Differences between the various algorithms are:

- The number of recorded interferograms.
- The phase shift between these interferograms.
- Susceptibility of the algorithm to errors in the phase shift or environmental noise such as vibration and turbulence.

An example is the (N+1)-bucket algorithm developed by Surrel [16], as the name says for N+1 images with a phase shift between each of the sequentially recorded images of:

$$\alpha = \frac{2\pi}{N} \quad (3.2)$$

So that between the first and the last image there is a phase difference of  $2\pi$ . The phase is obtained from:

$$\phi = \arctan \frac{\frac{I(0) - I(N)}{2} \cot\left(\frac{2\pi}{N}\right) - \sum_{n=1}^{N-1} I(n) \sin\left(\frac{2\pi n}{N}\right)}{\frac{I(0) + I(N)}{2} + \sum_{n=1}^{N-1} I(n) \cos\left(\frac{2\pi n}{N}\right)} \quad (3.3)$$

where  $I(n)$ , is the recorded intensity for a phase shift equal to  $n\alpha$ . This algorithm has two advantages, a large quantity of images could be acquired to improve the signal-to-noise ratio and is insensitive to phase shift miscalibration because an average of the first and the last

image is taken.

As we mention above, there are a wide variety of algorithms for calculating the phase using phase shifting technique. But contrary to what thought, different results could be obtained using different algorithms because some algorithms are more sensitive to a particular error sources than others, an example of the results obtained to compare some algorithms is in Ref. 7. An extensive revision of other algorithms and their properties could be found in Ref. 17. Anyway is important to make it clear that all of the algorithms are valid too for integrating-bucket technique.

There are numerous sources of error that affect the accuracy of phase measurements. The errors can be separated in three categories: (1) those associated with the data acquisition process, this includes errors in the phase shift process, nonlinearities in the detection system, amplitude and frequency stability of the source and quantization errors obtained in the analog-to-digital conversion process, (2) environmental effects, such as vibration and air turbulence and (3) those associated with defects in optical and mechanical design and fabrication. A detailed description of the error sources is in Ref. 5.

### 3.2 FOURIER TRANSFORM METHOD

The FTM is a well known method and widely used for obtaining phase, this method was developed for Takeda *et al.* [18], and a few years later the FTM was extended to the two-dimensional (2D) space [19, 20].

The intensity of a fringe pattern given by Equation 3.1 could be rewritten as:

$$g(x, y) = a(x, y) + b(x, y) \cos(\phi(x, y) + 2\pi f_0 x) \quad (3.4)$$

where  $f_0$  represent the carrier frequency.

To describe the FTM Equation 3.4 must be rewritten as:

$$g(x, y) = a(x, y) + c(x, y) e^{2\pi i f_0 x} + c^* e^{-2\pi i f_0 x} \quad (3.5)$$

where  $c(x, y) = \frac{1}{2}b(x, y)e^{i\phi(x, y)}$

First the Fourier transform of the interferogram, Equation 3.5, is taken with respect to  $x$ :

$$G(f, y) = A(f_x, y) + C(f_x - f_0, y) + C^*(f_x + f_0, y) \quad (3.6)$$

where capital letters denote Fourier spectra and  $f_x$  is the spatial frequency in  $x$  direction. Equation 3.6 represent a spectrum formed for one central lobe and two lobes that represent the high frequency of the image or the fringes, Figure 3.2A. Using a filter function any of the two spectra can be isolated and translated by  $f_0$  towards the origin to remove the carrier and obtain  $C(f_x, y)$ , Figure 3.2B.

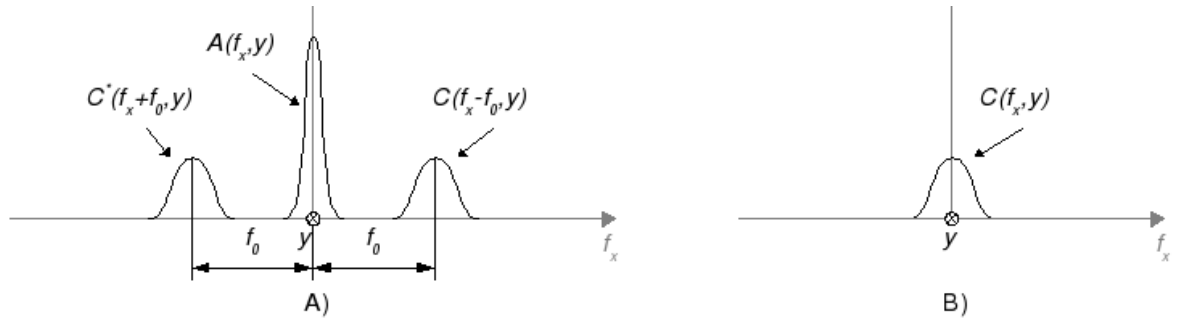


Figure 3.2 A) Separated Fourier spectrum of a fringe pattern, B) Single spectrum selected and translated to the origin.

Then the inverse Fourier transform of  $C(f_x, y)$  with respect to  $f_x$  is computed and as a result the complex function  $c(x, y)$  is obtained. Next, we calculate the complex logarithm of  $c(x, y)$ , to obtain:

$$\log[c(x, y)] = \log\left[\frac{1}{2}b(x, y)\right] + i\phi(x, y) \quad (3.7)$$

Finally, the phase is obtained by:

$$\phi(x, y) = \arctan \frac{\text{Im}[c(x, y)]}{\text{Re}[c(x, y)]} \quad (3.8)$$

where Re and Im represent the real and imaginary part of  $c(x, y)$ .

### 3.3 PHASE UNWRAPPING

The phase obtained by either method, phase shifting or FTM, is wrapped in modulo  $2\pi$  because the arc tangent function involved in the phase estimation process, Equations 3.3 and 3.8. Although the arc tangent function calculate the angle in the interval from  $-\pi/2$  to  $\pi/2$ , the signs of the numerator ( $\sin \phi$ ) and denominator ( $\cos \phi$ ) allow the calculation of the angle from  $-\pi$  to  $\pi$ . The relationship between the wrapped and unwrapped phase can be stated as:

$$\phi(x_i, y_j) = \phi_w(x_i, y_j) + 2\pi m(x_i, y_j); \quad 1 \leq i \leq N; \quad 1 \leq j \leq M \quad (3.9)$$

where  $\phi(x, y)$  is the unwrapped phase,  $\phi_w(x, y)$  is the wrapped phase, and  $m(x, y)$  is an integer-valued number known as the field number.  $M$  and  $N$  represent the rows and columns of the image in pixels, respectively.

When the recorded fringe patterns satisfy the Nyquist criteria [17] (at least two pixels per period), the phase unwrapping process is straightforward. Having at least two pixels per fringe implies that the phase changes by no more than  $\pi$  per pixel spacing. This criteria is used to reconstruct the phase map. Unwrapping process only require to compare the phase between adjacent pixels and add or subtract  $2\pi$  or multiples of  $2\pi$  when the difference is greater than  $\pi$ . After this operation discontinuities are removed, Figure 3.3.

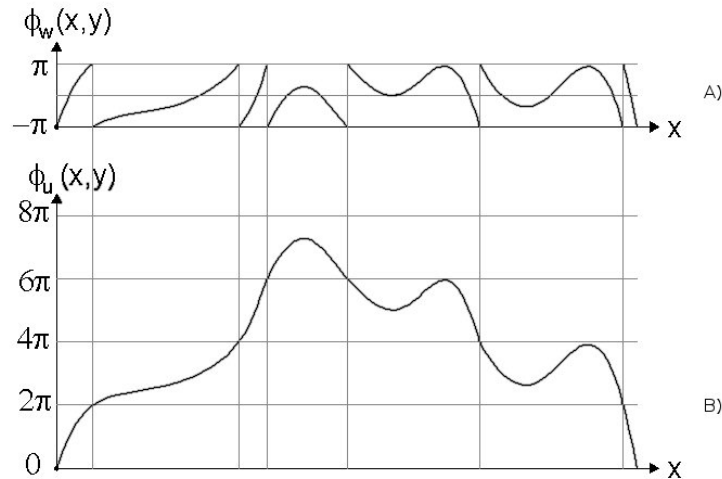


Figure 3.3 A) Example of a wrapped phase, and B) the unwrapped phase after remove discontinuities.



The unwrapping procedure consists of finding the correct field number for each phase measurement, Equation 3.9. Taking  $m(x_1)=0$ , this field number has only three possibilities at each pixel [17, 21]:

$$\begin{aligned}
 m(x_1) &= 0 \\
 m(x_i) &= m(x_{i-1}) \quad \text{if } |\phi_w(x_i) - \phi_w(x_{i-1})| < \pi \\
 m(x_i) &= m(x_{i-1}) + 1 \quad \text{if } \phi_w(x_i) - \phi_w(x_{i-1}) \leq -\pi \\
 m(x_i) &= m(x_{i-1}) - 1 \quad \text{if } \phi_w(x_i) - \phi_w(x_{i-1}) \geq \pi
 \end{aligned} \tag{3.10}$$

$$i = 2, 3, \dots, N$$

Several authors [17, 21, 22] have also described methods for unwrapping in one and two dimensions. A difficult situation arises when the absolute phase difference between adjacent pixels at points other than discontinuities in the arctangent function are greater than  $\pi$ , problem known as erroneous discontinuities or phase inconsistencies. This discontinuities can be introduced by

- High-frequency, high-amplitude noise.
- Discontinuous phase jumps.
- Regional undersampling in the fringe pattern.

### 3.3.1 Unwrapping consistent phase maps

Unwrap consistent phase map is the easiest case, we describe two simple techniques to apply to this case: (1) full-field wrapped phase data, and (2) wrapped phase data within an arbitrary simple connected region.

For the first case we briefly describe a technique that consists of integrating phase differences along a scanning path. Assuming that the full-field phase map is given by  $\phi_w(x, y)$  in a regular lattice of size  $M \times N$  pixels. We can unwrap this phase map by unwrapping the first row ( $j=0$ ) of it and afterward taking the last value of it as our initial condition to unwrap along the following row of the phase map in opposite direction and so on, Figure 3.4. We can do this by using the following formulas:

$$\begin{aligned}
 \phi(x_{i+1}, y_j) &= \phi(x_i, y_j) + V[\phi_w(x_{i+1}, y_j) - \phi(x_i, y_j)]; \quad 0 \leq i \leq N-2 \\
 \phi(x_{N-1}, y_{j+1}) &= \phi(x_{N-1}, y_j) + V[\phi_w(x_{N-1}, y_{j+1}) - \phi(x_{N-1}, y_j)]
 \end{aligned} \tag{3.11}$$

$$\begin{aligned}\phi(x_{i-1}, y_{j+1}) &= \phi(x_i, y_{j+1}) + V[\phi_w(x_{i-1}, y_{j+1}) - \phi(x_i, y_{j+1})]; & 1 \leq i \leq N-1 \\ \phi(x_0, y_{j+2}) &= \phi(x_0, y_{j+1}) + V[\phi_w(x_0, y_{j+2}) - \phi(x_0, y_{j+1})]\end{aligned}\quad (3.12)$$

where the wrapping function is  $V(x) = \arctan(\sin(x)/\cos(x))$ , valid in the interval  $(-\pi, \pi)$ . The scanning procedure described starts in  $j=0$ , as mentioned above, and it is followed by incrementing  $j=2$  until the full-field phase map is unwrapped. In Equation 3.11 we can use as our initial condition  $\phi(x_0, y_0) = \phi_0$ .

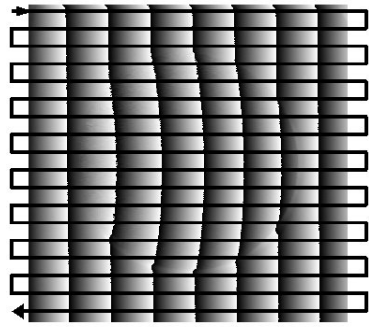


Figure 3.4 Path followed by the proposed algorithm.

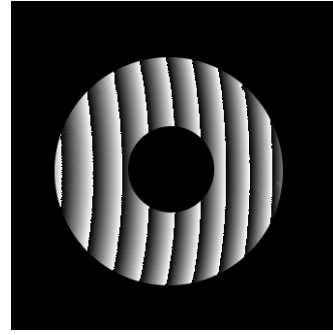


Figure 3.5 Example of a simple connected region containing valid phase data.

For the second case become necessary to define and set to zero an indicator function  $\sigma(x, y)$ , inside the domain  $(D)$  of valid phase data, Figure 3.5.

Then, choose a starting point inside  $D$  and assign to it an arbitrary phase value of  $\phi(x, y) = \phi_0$ . Mark the visited site as unwrapped; that is  $\sigma(x, y) = 1$ . One time that the first pixel is defined, we can carry out the unwrapping process, that consist in choose a pixel inside  $D$  (in any order) and test if the visited site is wrapped and if any adjacent pixel has already been unwrapped, if so the unwrapped pixel is used to unwrap the current pixel, and the site is marked as unwrapped, and another pixel is tested. When any condition is not fulfilled become necessary to test another pixel. The process is repeated until every pixel inside  $D$  is marked as unwrapped.

### 3.3.2 Unwrapping inconsistent phase maps

Unfortunately some phase maps have errors as mentioned above and the algorithms described

in the preceding section do not work. Although many algorithms for this problem have been proposed, we will limit ourselves to briefly present the technique for 2D unweighted least-squares phase unwrapping developed by Ghiglia [23].

We need to determine the unwrapped phase values  $\phi(x, y)$  from Equation 3.9, with the requirement that the phase differences of the  $\phi(x, y)$  agree with those of  $\phi_w(x, y)$  in the least-square sense. First, we define a wrapping operator  $W\{\phi\}=\phi_w$  that wraps all values of its argument into the range  $(-\pi, \pi)$ .

Next, we compute two sets of phase differences: those differences with respect to the  $i$  index and those with respect to the  $j$  index. Specifically, from our known values of the wrapped phase  $\phi_w(x, y)$ , we compute the following wrapping differences:

$$\begin{aligned}\Delta_{i,j}^x &= W\{\phi_w(x_{i+1}, y_j) - \phi_w(x_i, y_j)\}; & i=1,2,\dots,M-1; \quad j=1,2,\dots,N \\ \Delta_{i,j}^x &= 0; & \text{otherwise} \\ \Delta_{i,j}^y &= W\{\phi_w(x_i, y_{j+1}) - \phi_w(x_i, y_j)\}; & i=1,2,\dots,M; \quad j=1,2,\dots,N-1 \\ \Delta_{i,j}^y &= 0; & \text{otherwise}\end{aligned}\tag{3.13}$$

where  $x$  and  $y$  superscripts refer to differences in the  $i$  and  $j$  indices, respectively.

The relationship between the wrapped phase differences, Equations 3.13, and the unwrapped phase values  $\phi(x, y)$ , in the least-squares-error sense is given by:

$$\begin{aligned}\phi(x_{i+1}, y_j) + \phi(x_{i-1}, y_j) + \phi(x_i, y_{j+1}) + \phi(x_i, y_{j-1}) - 4\phi(x_i, y_j) = \\ \Delta_{i,j}^x - \Delta_{i-1,j}^x + \Delta_{i,j}^y - \Delta_{i,j-1}^y\end{aligned}\tag{3.14}$$

where

$$\rho(x_i, y_j) = \Delta_{i,j}^x - \Delta_{i-1,j}^x + \Delta_{i,j}^y - \Delta_{i,j-1}^y\tag{3.15}$$

Compute the forward 2D discrete cosine transform (DCT) of Equation 3.15, to yield the 2D DCT values  $\hat{\rho}(x_i, y_j)$ . Calculate  $\hat{\phi}(x_i, y_j)$  from:

$$\hat{\phi}(x_i, y_j) = \frac{\hat{\rho}(x_i, y_j)}{2\left(\cos\frac{\pi i}{M} + \cos\frac{\pi j}{N} - 2\right)}\tag{3.16}$$

Finally perform the 2D inverse DCT of Equation 3.16 to obtain the least-squares unwrapped

phase values  $\phi(x, y)$ . Note that Equation 3.16 is indeterminate for  $i=0$  and  $j=0$ , usually  $\hat{\phi}(x_0, y_0) = \hat{\rho}(x_0, y_0)$  to leave the bias unchanged.

## REFERENCES

1. Malacara D., DeVore S.L., "Interferogram Evaluation and Wavefront Fitting", *Optical Shop Testing*, Malacara D., Editor, Wiley, New York (1992)
2. Kwon O.Y., "Multichannel Phase-Shifted Interferometer", *Opt. Lett.*, **9**, pp. 59-61 (1984)
3. Kwon O.Y., Shough D.M., Williams R.A., "Stroboscopic Phase-Shifting Interferometry", *Opt. Lett.*, **12**, pp. 855-857 (1987)
4. Kujawinska M., Robinson D.W., "Multichannel Phase-Stepped Holographic Interferometry", *Appl. Opt.*, **27**, pp. 312-320 (1988)
5. Greivenkamp J.E., Bruning J.H., "Phase Shifting Interferometry", *Optical Shop Testing*, Malacara D., Editor, Wiley, New York (1992)
6. Gasvik K.J., *Optical Metrology*, Chapter 11, Wiley, England (2003)
7. Creath K., "Phase-Measurement Interferometry Techniques", *Progress in optics, Vol. XXVI*, Wolf E., Editor, Elsevier, Amsterdam (1988)
8. Crane R., "Interference Phase Measurement", *Appl. Opt.*, **8**, pp 538-542 (1969)
9. Koliopoulos C.L., "Radial Grating Lateral Shear Heterodyne Interferometer", *Appl. Opt.*, **19**, pp. 1523-1528 (1980)
10. Sommargren G.E., "Optical Heterodyne Profilometry", *Appl. Opt.*, **20**, pp. 610-618 (1981)
11. Barnes T.H., "Heterodyne Fizeau Interferometer for Testing Flat Surfaces", *Appl. Opt.*, **26**, pp. 2804-2809 (1987)
12. Moore D.T., Murray R., Neves F.B., "Large Aperture AC Interferometer for Optical Testing", *Appl. Opt.*, **17**, pp. 3959-3963 (1978)
13. Wyant J.C., Shagam R.N., "Use of Electronic Phase-Measurement Techniques in Optical Testing", *Proc. ICO II: Optica Hoy y Mañana*, Bescos J., Hidalgo A., Plaza L., Santamaria J., Editors, Madrid (1978)
14. Moore D.T., Truax B.E., "Phase-Locked Moiré Fringe Analysis for Automated Contouring

- of Diffuse Surfaces”, *Appl. Opt.*, **18**, pp. 91-96 (1979)
15. Matthews H.J., Hamilton D.K., Sheppard C.J., “Surface Profiling by Phase-Locked Interferometry”, *Appl. Opt.*, **25**, pp. 2372-2374 (1986)
  16. Surrel Y., “Phase Stepping: A New Self-Calibrating Algorithm”, *Appl. Opt.*, **32**, pp. 3598-3600 (1993)
  17. Malacara D., Servin M., Malacara Z., *Interferogram Analysis for Optical Testing*, Chapters 2 and 11, Taylor & Francis, Boca Raton (2005)
  18. Takeda M., Ina H., Kobayashi S., “Fourier-Transform Method of Fringe-Pattern Analysis for Computer-Based Topography and Interferometry”, *J. Opt. Soc. Am.*, **72**, pp. 156-160 (1982)
  19. Nugent K.A., “Interferogram Analysis Using an Accurate Fully Automatic Algorithm”, *Appl. Opt.*, **24**, pp. 3101- 3105 (1985)
  20. Bone D.J., Bachor H.A., Sandeman R.J., “Fringe-Pattern Analysis Using a 2-D Fourier Transform”, *Appl. Opt.*, **25**, pp. 1653-1660 (1986)
  21. Kreis T. “Digital Holographic Interference-Phase Measurement Using the Fourier Transform Method”, *J. Opt. Soc. Am. B*, **3**, pp. 847-855 (1986)
  22. Ghiglia D.C., Pritt M.D., *Two-Dimensional Phase Unwrapping: Theory, Algorithms and Software*, Wiley (1998)
  23. Ghiglia D.C., Romero L.A., “Robust Two-Dimensional Weighted and Unweighted Phase Unwrapping That Uses Fast Transforms and Iterative Methods”, *J. Opt. Soc. Am. A*, **11**, pp. 107-117 (1994)

## CHAPTER 4

### ANALYSIS OF GRATING PERIOD IN FRINGE PROJECTION TECHNIQUE

---

Fringe projection technique is used to obtain the 3D shape of an object. When a sinusoidal fringe pattern is projected onto a test surface, the intensity distribution of the deformed fringe pattern that is observed through a camera can be described by Equation 3.4. From the fringe analysis, such as phase shifting or FTM, the modulated phase could be obtained. After demodulation of phase, 3D information about the surface can be recovered of a phase-to-depth-conversion. This relationship involves the parameters of the imaging system, the inaccuracy in measuring the experimental parameters is the main source of the systematic errors [1].

Systematic errors are not the only cause of error. Almost all phase shifting algorithms are designed for sinusoidal fringes, unfortunately in practice the fringe pattern often become nonsinusoidal [2] and is not described by Equation 3.4 as we mention above, so the algorithms give residual errors in calculated phase due to higher harmonic components. Phase detection of nonsinusoidal signals is treated by Malacara *et. al.* [3].

In digital fringe projection, if ideal sinusoidal fringe pattern is sent to projector, the fringe image produced by the projector is nonsinusoidal [4]. Even if a sinusoidal fringe pattern is projected over the object, distortion may appear for many reasons, for example: the discrete sampling of the camera, the nonlinear response of the light detector with the signal, and the noise introduced in the measurement by the optical system. In this chapter we present the analysis of the error introduced in 3D shape reconstruction due to the lost of sinusoidality of the signal, and the influence of the period of the projected grating.

## 4.1 INTRODUCTION

A real, infinitely extended periodic function can be represented by Fourier series. Let us consider a band-limited real function  $g(x)$  whose spectrum is  $G(f)$ . The width,  $\Delta f$ , of this spectrum is equal to the maximum frequency  $f_{max}$  contained in the function. To sample the function  $g(x)$  we need to multiply this function by the comb function  $h(x)$ , with fundamental frequency known as the sampling frequency  $f_s$ .

If the sampling frequency of the function  $h(x)$  decreases, the spectral elements in the convolution of the functions  $G(f)$  and  $H(f)$  get closer to each other. If these spectral elements are completely separated without any overlapping, the inverse Fourier transforms recovers the original function with full detail and frequency content. If the spectral elements overlap each other the process is not reversible and the original function may not be fully recovered after sampling.

Hence the sampling frequency must be greater than twice the maximum frequency contained in the signal or function to be sampled:

$$f_s > 2f_{max}.$$

This condition is known as the *Whittaker-Shannon sampling theorem*, and the minimum sampling frequency is referred to as the *Nyquist frequency*.

We have assumed that the interval sampling function  $h(x)$  extends from  $-\infty$  to  $+\infty$ . When the sampling function extends only to a limited interval, is equivalent to multiply the function  $g(x)$  by a window function  $w(x)$ , before sampling. The spectrum  $W(f)$  of the window function is a sinc function, as a consequence the spectrum of the sampled function have some overlap and perfect recovery is not possible, as in most practical cases.

There is only one exception will limited sampling leads to perfect recovery of the function. If the sampled signal is periodic we may assume that the sampling pattern repeats itself outside the sampling interval. A sampling interval with length equal to the period of the function and the sampling points equally distributed is enough to obtain full recovery of the function,

because sampling may be mathematically considered as extending to the entire interval  $-\infty$  to  $+\infty$ .

We have consider the sampling of a periodical function using a detector that measures the signal at one value of the phase; however, real detectors have finite size and take the average value in one small phase interval.

When recording the image of a fringe pattern with a detector array, such as a CCD, the intensity over each pixel is averaged and displayed as a gray level value. The effect of this signal averaging reduces the contrast of the fringes, as the averaging interval increases the contrast reduction increases, Figure 4.1. When the averaging interval is a multiple of the period of the signal, the contrast is reduced to zero and no signal is detected, but the DC component is detected [3].

Figure 4.1 shows a sinusoidal signal sampled with a frequency: A) high than twice the frequency of this signal, three points per period, B) equal to the frequency of this signal, C) less than the frequency of this signal and D) lower than the frequency of this signal, one sample per period.

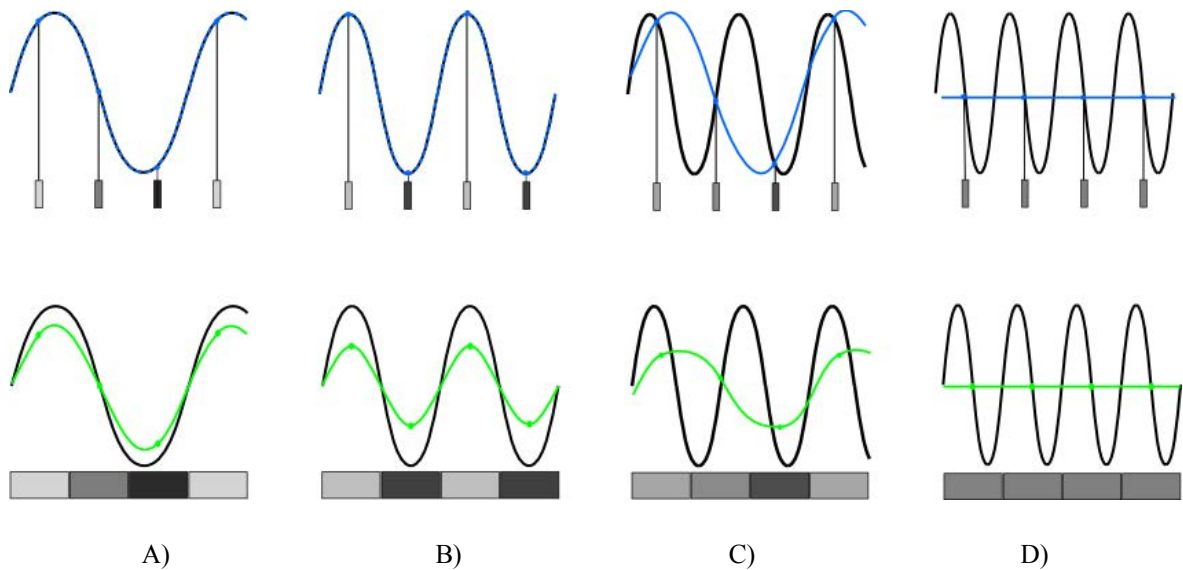


Figure 4.1 Contrast of a detected signal for a finite size of integration. The upper line is for small integration interval, and the lower line for large integration interval. A)  $f_s > 2f_{\max}$ , B)  $f_s = 2f_{\max}$ , C)  $f_s < 2f_{\max}$  and D)  $f_s \ll 2f_{\max}$ .



This averaging process also may distort the signal (Figure 4.2, continuous line), causing loss of sinusoidality in the fringe profile (Figure 4.2, dotted line), even the distortion varies depending of the position of the signal over the pixel array. The loss of sinusoidality when the fringes are detected introduce an error in the resulting phase.

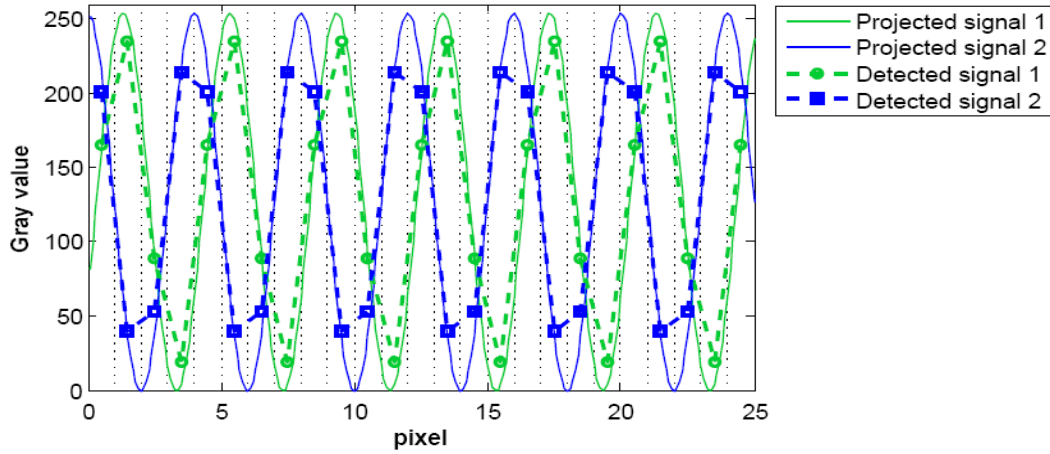


Figure 4.2 Distortion of two signals of equal period,  $p=4 \text{ pix/fringe}$ , and a phase shift between them.

When a wide section of a signal falls over one pixel is equivalent to have a large averaging interval, and the distortion increases due to the averaging process. To avoid distortion effects the signal has to be sampled by an appropriate quantity of pixels. As a small part of the signal falls over the pixel the signal detected by the camera fits better to the original signal, Figure 4.2 and 4.3.

## 4.2 EXPERIMENT

The surface under test was a semi-spheric object. The radius of curvature of the object was measured using a spherometer described in Appendix A. In order to determine the error obtained with different grating periods  $p_1, p_2, \dots, p_5$ , the object topography is obtained by fringe projection technique using CGGs and compared with a reference surface generated from physical measurements obtained with the spherometer.

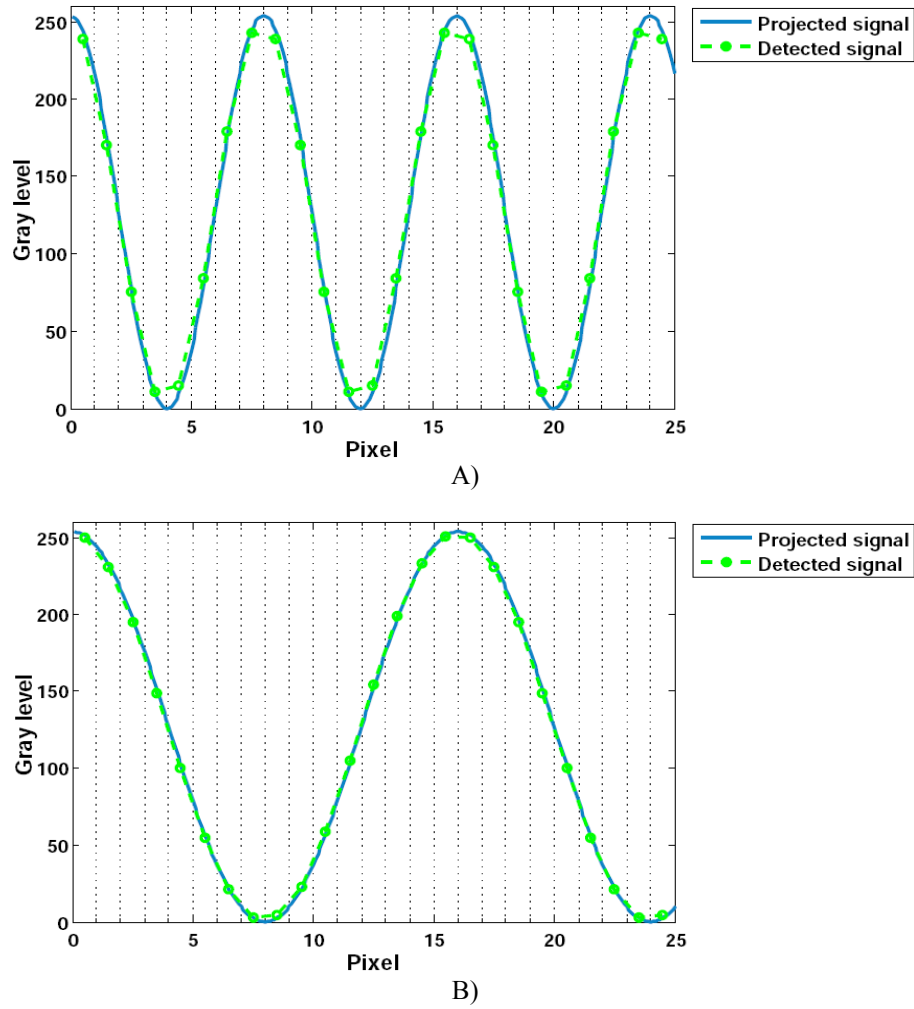


Figure 4.3 Distortion of a signal with period: A)  $p=8$  and B)  $p=16$  pix/fringe.

The experimental arrangement for 3D shape measurement is shown in Figure 4.4. For the projection of CGGs a single-chip digital light processing (DLP) projector of  $800 \times 600$  pixels is used. The acquisition of the deformed fringe patterns is made with a charge-coupled-device (CCD) monochromatic camera with a resolution of  $640 \times 480$  pixels. The view axis is normal to the reference plane. The projector and the camera are placed at a distance  $L=79.95$  cm from the reference plane. The angle between the projector and the camera is  $\alpha_0=11.54^\circ$ , Figure 4.5. The lateral resolution obtained was  $0.196$  mm. The observation area was  $66.6 \times 66.6$  mm.



Figure 4.4 Experimental set up for three-dimensional shape measurement: 1. Projector, 2. Object, 3. CCD camera, and 4. PC.

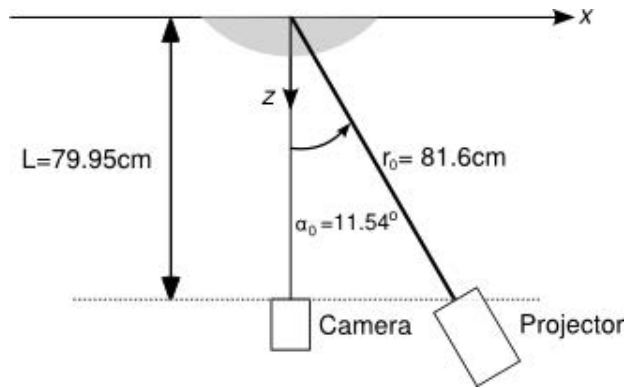


Figure 4.5 Schematic diagram of the experimental set up.

Sinusoidal gratings of periods 4, 8, 12, 16 and 20 *pix/fringe* were generated. These were projected on the object surface to obtain the topography with each one of pitch. Due to the sampling process and the noise of the camera, the profile of the observed fringes is nonsinusoidal, Figure 4.6.

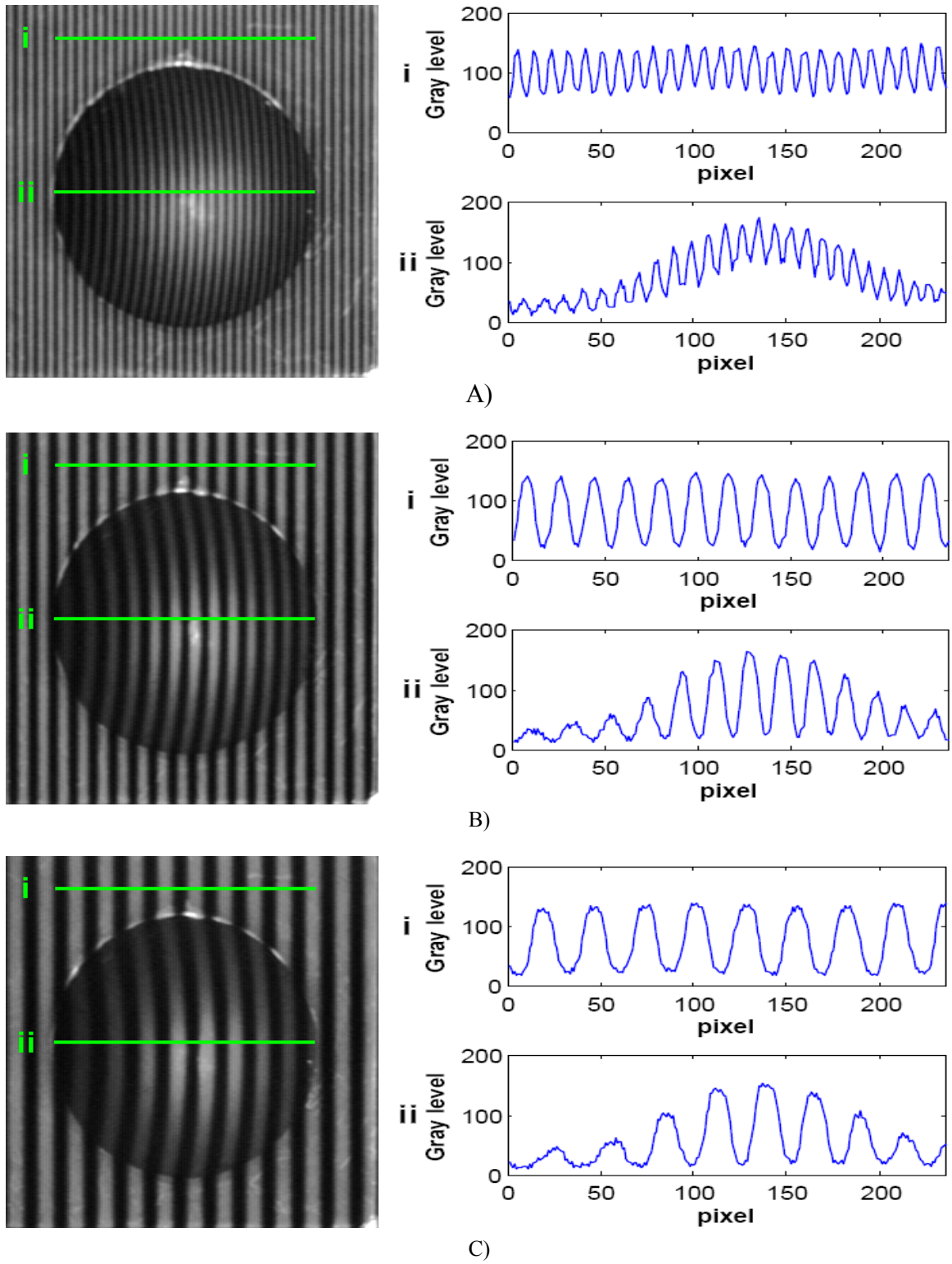


Figure 4.6 Profile of projected fringes on the object surface, for a projected grating of periods: A)  $p_1=4$ , B)  $p_2=8$ , and C)  $p_3=12$  pixels/fringe, respectively.

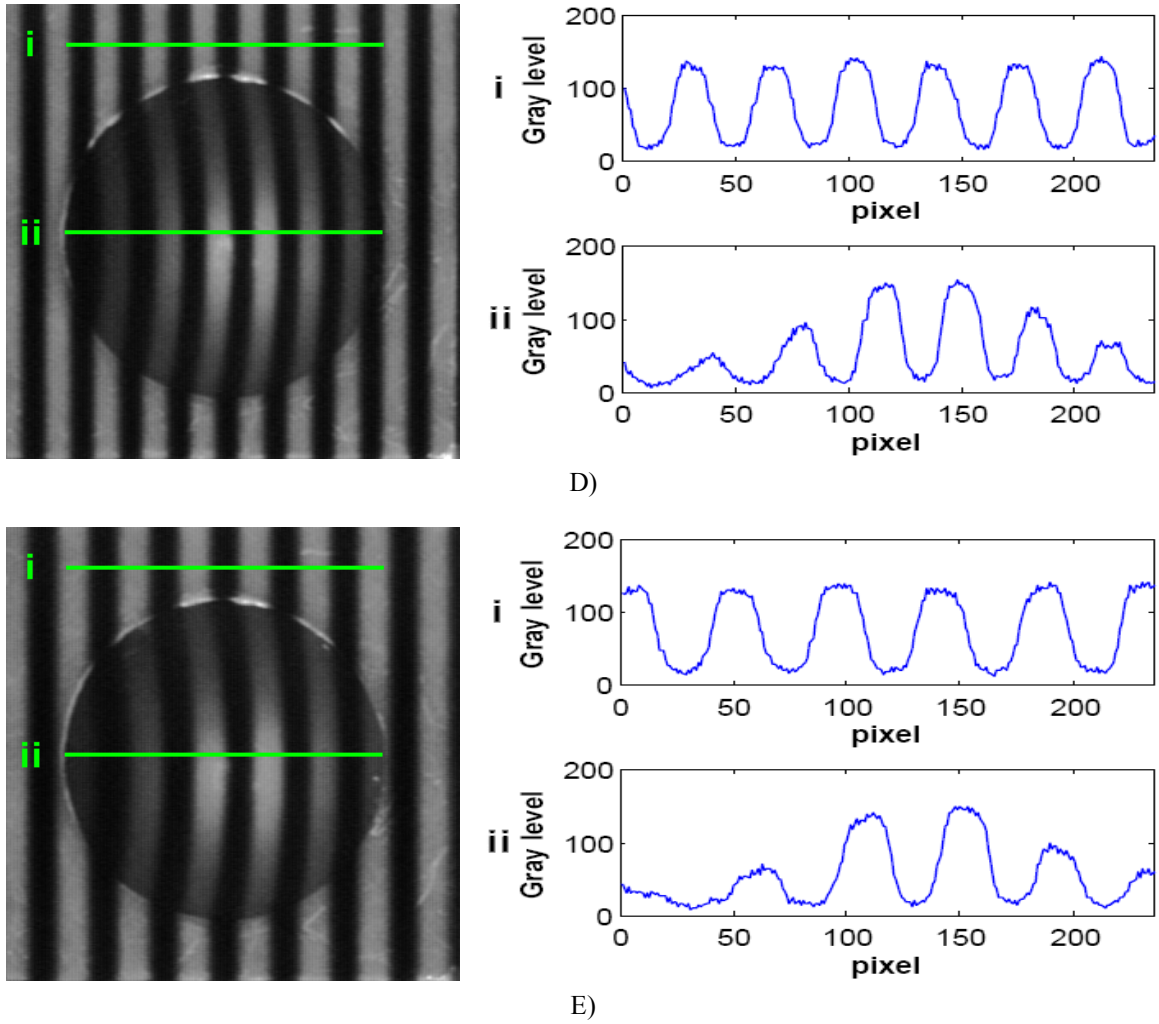


Figure 4.6 (continued) Profile of projected fringes on the object surface, for a projected grating of periods:  
D)  $p_4=16$  and E)  $p_5=20$  *pix/fringe*, respectively.

The phase shifting technique was used to (N+1)-bucket algorithm, Equation 3.3, for  $N=16$  images. The shift of CGGs is made via software eliminating the possibility of phase shift errors. The phase obtained is in modulo  $2\pi$ , Figure 4.7A, and then an unwrapping process is required. One time that the phase has been demodulated, we subtract the measured phase map of the object from measured phase map of a reference planar surface at  $z=0$ . Finally the height of the object is obtained by Equation 2.16. Figure 4.7B shows the topography when the grating pitch is  $8$  *pix/fringe*.

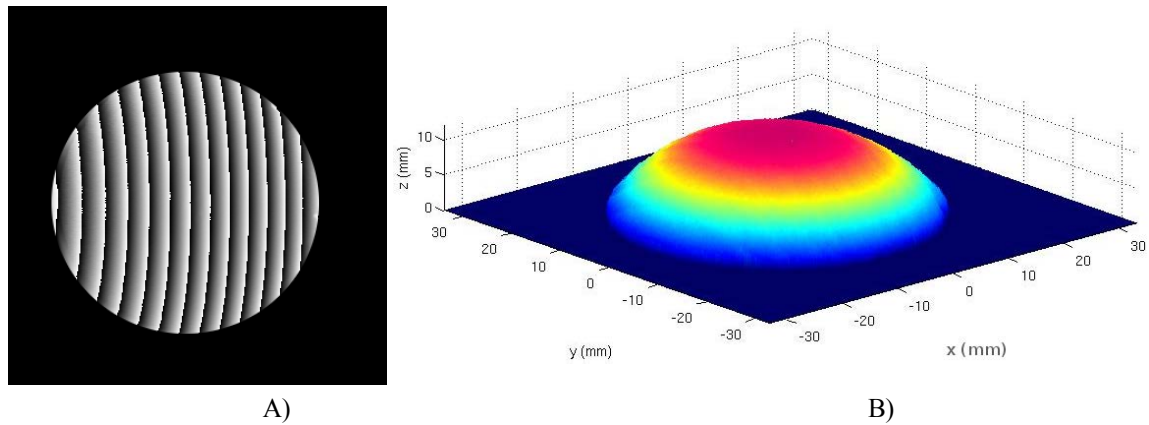


Figure 4.7 A) Wrapped phase and B) Three-dimensional shape, for grating period  $p_2 = 8$  pix/fringe.

In order to determine the error obtained for each grating period, we calculate the standard deviation of the difference between the obtained topography by fringe projection technique and the reference surface by using spherometer, Table 4.1.

Grating	Period of the projected grating (pix/fringe)	Period of the observed grating (pix/fringe)	Error (mm)
p1	4	9.03	0.4988
p2	8	18.04	0.1358
p3	12	27.17	0.1684
p4	16	36.13	0.2245
p5	20	45.25	0.2347

Table 4.1 Error of the topography obtained

When the grating period is incremented, the fringe profile becomes more sinusoidal. However, this occurs in the interval *8 to 12 pixel/fringe*. To larger periods occur lost of sinusoidality. The deviation from the reference surface increases due to the illumination produces unwanted shadows on the object surface. This causes lost of sinusoidality in the left side of the object, Figure 4.6 and 4.8. These results indicate that the grating period should be enough large to observe a sinusoidal profile, but at the same time appropriate to give the necessary information of the object. In other words, the projected fringes pitch must be selected from an interval. Of course a perfect sinusoidal profile can not be achieved due to the noise of the camera.



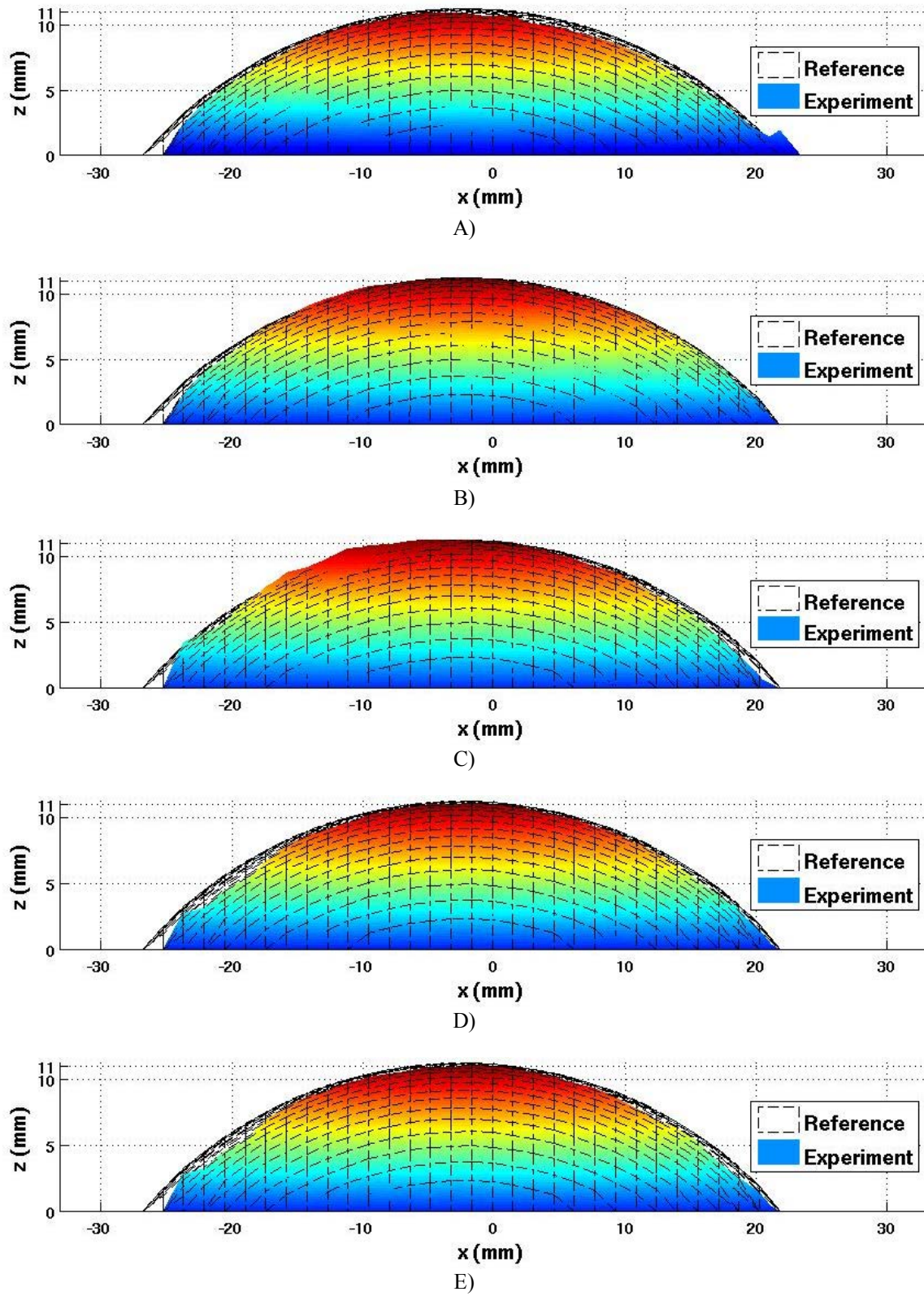


Figure 4.8 Comparison between topography obtained by fringe projection against the reference surface which was measured with a spherometer. The period of the projected gratings is: A)  $p_1=4$ , B)  $p_2=8$ , C)  $p_3=12$  pix/fringe, D)  $p_4=16$ , and E)  $p_5=20$  pix/fringe, respectively.

### 4.3 CONCLUSION

We present an analysis of the variation in the topography measured by fringe projection technique when different grating periods are used. The results shown that the ideal period on the reference plane should be between *15-30 pix/fringe*, these results were reported in Ref 5. The analysis shows the importance of determine the optimum period of the projected grating to adequately sample the object and minimizing the error in the result.

### REFERENCES

1. Zhang Z., Zhang D., Peng X., "Performance Analysis of a 3D Full-Field Sensor Based on Fringe Projection", *Opt. Lasers Eng.*, **42**, pp. 341-353 (2004)
2. Hibino K., Oreb B.F., Farrant D.I., "Phase Shifting for Nonsinusoidal Waveforms with Phase-Shift Errors", *J. Opt. Soc. Am. A*, **12**, pp. 761-768 (1995)
3. Malacara D., Servin M., Malacara Z., *Interferogram Analysis for Optical Testing*, Chapters 2, 5 and 6, Taylor & Francis, Boca Raton (2005)
4. Zhang S., Huang P.S., "Phase Error Compensation for a 3-D Shape Measurement System Based on the Phase Shifting Method", *Opt. Eng.*, **46**, 063601 (2007)
5. León-Huerta A., Martinez Amalia, Rayas J.A., Puga H.J., "Influencia del Periodo de Franjas Proyectadas en la Medición de la Topografía de Objetos", *V Encuentro Participacion de la Mujer en la Ciencia*, ISBN 978-968-9241-04-1, S2-FMC T14, México (2008)



## **CHAPTER 5**

### **DYNAMIC MEASUREMENT OF OUT-OF-PLANE DEFORMATION IN TEST**

#### **SPECIMEN BY FRINGE PROJECTION**

---

By using fringe projection technique and FTM, the out-of-plane dynamic deformation measurements of sheet metal specimens subjected to uniaxial tensile test is obtained. We measure the displacement field in the elastic and plastic zones during its elongation until fracture took place. The mechanical behavior of two different materials, stainless steel and hot rolled steel are studied. Analysis of material behavior under loading is important due to development of new materials. The technique is applied to metal samples, that have a well known and widely studied behavior, but it can be applied to any other material, as composites, or even to a manufactured members like sheet metal forming.

#### **5.1 INTRODUCTION**

The study of mechanic fractures is very important due to the damage caused when complex structures collapse. Usually existing procedures are enough to avoid failure, but negligence during design, construction or operation of structure could cause failure. However the application of a new design or material can produce an unexpected and undesirable result. When an improved design is introduced, there are invariably factors that the designer does not anticipate. New materials can offer tremendous advantages, but also potential problems.

Nowadays metals are being replaced with plastics, ceramics, and composites in a wide number of applications. Some of the main advantages of engineering plastics are low cost, ease fabrication, and corrosion resistance. Ceramics provide superior wear resistance and creep strength. Composites offer high strength/weight ratios, and enable engineering to design materials with specific elastic, thermal and direction-dependent properties [1].

Nonmetals, like metals, are not immune to fracture. The procedure of testing metals is well established, but for nonmetals research of fracture behavior is beginning. A tensile test consists in measuring the deformation of a straight bar undergoing an axial load by using a testing machine. Specimen dimensions and testing methods are well established by various standard organizations like the American Society of Testing Materials (ASTM). Some mechanical properties of materials can be determined from the stress-strain diagram obtained from the tensile test, because the elastic and plastic zones of a material are located. The stress-strain diagram was described in chapter 1, Figure 1.3.

When an axial load is applied to the specimen, it elongates. Electromechanical extensometers are mounted on the specimen to measure the change in length. This is a way of measuring local in-plane displacement by means of mechanical sensors. Although the behavior of a metallic specimen undergoing tension is well known, there is not any mechanical method to measure out-of-plane deformation of the specimen. During a tensile test, precise load increments and testing velocity must be carefully chosen, since material properties are quite sensitive to the rate of loading. At high rates, for example, inertia effects and material rate dependence can be significant.

Although many aspects of testing are similar for metals and nonmetals, there are several important differences because some materials exhibit a nonlinear time-dependent behavior such as viscoplasticity and viscoelasticity. Mechanical behavior of plastics can be highly time-dependent. Composites are in general discrete, piecewise nature with sharp interfaces. This results in abrupt transitions on their thermal, mechanical and physical properties. Commonly, these interfaces contain some defects due to imperfect bonding, residual stresses, etc. The mismatch in properties across the interfaces leads to stress concentration and consequently the interfaces become a favored site of cracking, debonding and spallation [2].

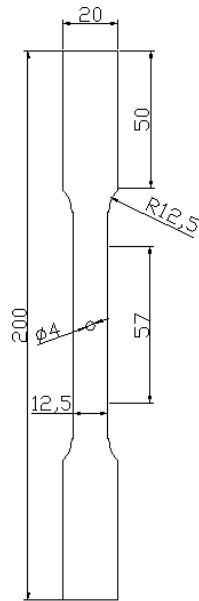
## 5.2 EXPERIMENT

Metal sheet samples of stainless steel (SS) and hot rolled steel (HRS) are subjected to tensile test. The samples have different thickness as described in Table 5.1 and were manufactured according to the ASTM E8 testing standard [3]. To induce fracture in a specific region of the sample a circular hole of 4 mm diameter was drilled at the geometrical center, since this area presents a high stress concentration. The dimensions of the specimens are shown in Figure 5.1A.

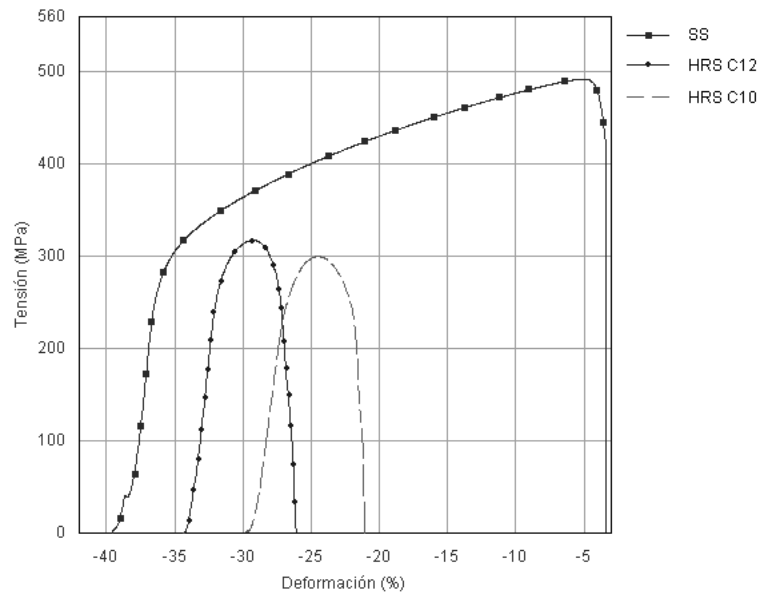
Material	Thickness (mm)	Loading rate (mm/min)	Final Length (mm)	Elongation %
Stainless Steel	1.90	10	216	8.0
Hot Rolled Steel C2	2.66	8	203	1.5
Hot Rolled Steel C10	3.42	8	202	1.0

\*C12 and C10 refers to thickness

Table 5.1 Specimen specifications.



A)



B)

Figure 5.1 A) Specimen dimensions in mm, and B) Stress-strain diagram obtained from the tensile test.

By using an Instron universal testing machine a uniaxial tensile load is applied along the  $y$  direction, at a rate of load of  $10$  and  $8 \text{ mm/min}$  on SS and HRS respectively. The load, elongation, stress and strain are indicated by the display device of the testing machine, from these data a variety of graphs can be constructed, including a stress-strain diagram, Figure 5.1B.

The applied load produces in-plane and out-of-plane deformations, in order to follow the changes of the samples topography induced by the deformation we use fringe projection technique. A binary CGG of period  $2 \text{ pix/fringe}$  is projected onto the specimen surface by a single-chip DLP projector of  $1024 \times 768 \text{ pixels}$ , the period was selected in order to have the major quantity of fringes over the surface. The acquisition of the deformed fringe patterns is with a CCD camera of  $640 \times 480 \text{ pixels}$ , placed at a distance  $L=39 \text{ cm}$  from the reference plane on optical axis. The angle between the projector and the camera is  $\alpha_0=30.6^\circ$ , obtaining a lateral resolution of  $0.045 \text{ mm}$ . Our observation area is  $21.36 \times 12.80 \text{ mm}$ . The experimental setup is shown in Figure 5.2A.

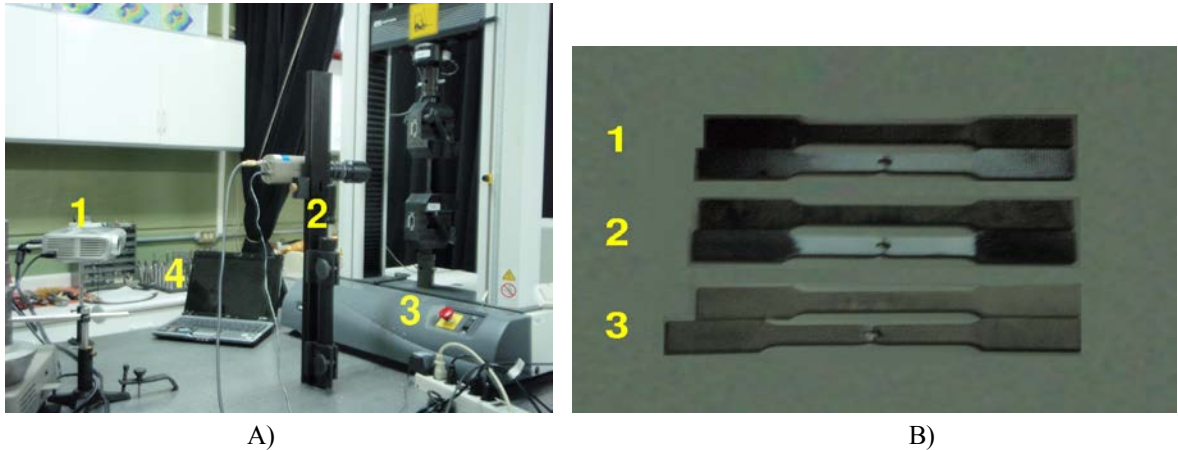


Figure 5.2 A) Experimental setup: 1. Projector, 2. CCD camera, 3. Testing machine and specimen and 4. PC, B) Elongated specimens after testing compared to non tested samples: 1. HRS C10, 2. HRS C12 and 3. SS.

Images that can be displayed in a monitor and are recorded by a camera with a video frame rate  $5 \text{ fps}$ . Too, they are stored in a digital frame storage card for their processing. The sample was subjected to a continue load and images were recorded at intervals of  $200 \text{ ms}$ . One time that the test starts, a sequence of images is taken at the given rate, to follow the out-of-plane

deformations of each specimen until the fracture occurs, Figures 5.3-5.5. The phase is obtained using the FTM. However due to the geometry of our specimens (with hole) we have non full-field fringe patterns and before applying the FTM is necessary extrapolate fringes outside the boundaries by the method described in Appendix B to avoid errors in phase detection because of boundary problems associated to Fourier transform. The phase obtained is in modulo  $2\pi$ , before the unwrapping process the unwanted information is removed from the phase map by a mask generated from the original image. Once the phase has been demodulated, we subtract it from the phase of the reference image and finally the deformation of the object is obtained by Equation 2.16.

The behavior of specimens in each zone is successfully followed. Special attention is paid in the failure process, which takes place before necking begins, Figures 5.3-5.5. As expected both materials, SS and HRS, exhibit different behavior due to their mechanical properties, specially at the fracture process.

SS alloys have low proportionality limits and extended strain-hardening capability. As shown in Figure 5.1B, for the SS sample, the plastic zone is quite large. Even suddenly the fracture occurs, Figure 5.3E and F, due to mechanical properties of the material. From Table 5.1 and Figure 5.2B we can notice that the elongation is large, about 8%, and the hole is displaced while enlarging. Near the fracture point, the sample exhibits a weak necking and an abrupt failure, in less than 0.2 sec.

Figure 5.1B also shows the results for the HRS samples. They present a small plastic zone and has a progressive fracture process, Figure 5.4E-H and Figure 5.5E-H, because the slope is small after the ultimate strength. From Table 5.1 we can appreciate that the elongation is proportional to 1% (dependent on thickness), the hole stays at the same position, but it is elongated. The specimen exhibits a lot of necking, and the fracture takes place slowly, about 0.8 sec for C12 and 1.5 sec for C10. Although both HRS specimens were tested in same conditions, due to their different thickness the fracture occurred faster for C12 sample, about 3.2 sec before the fracture of C10 specimen.

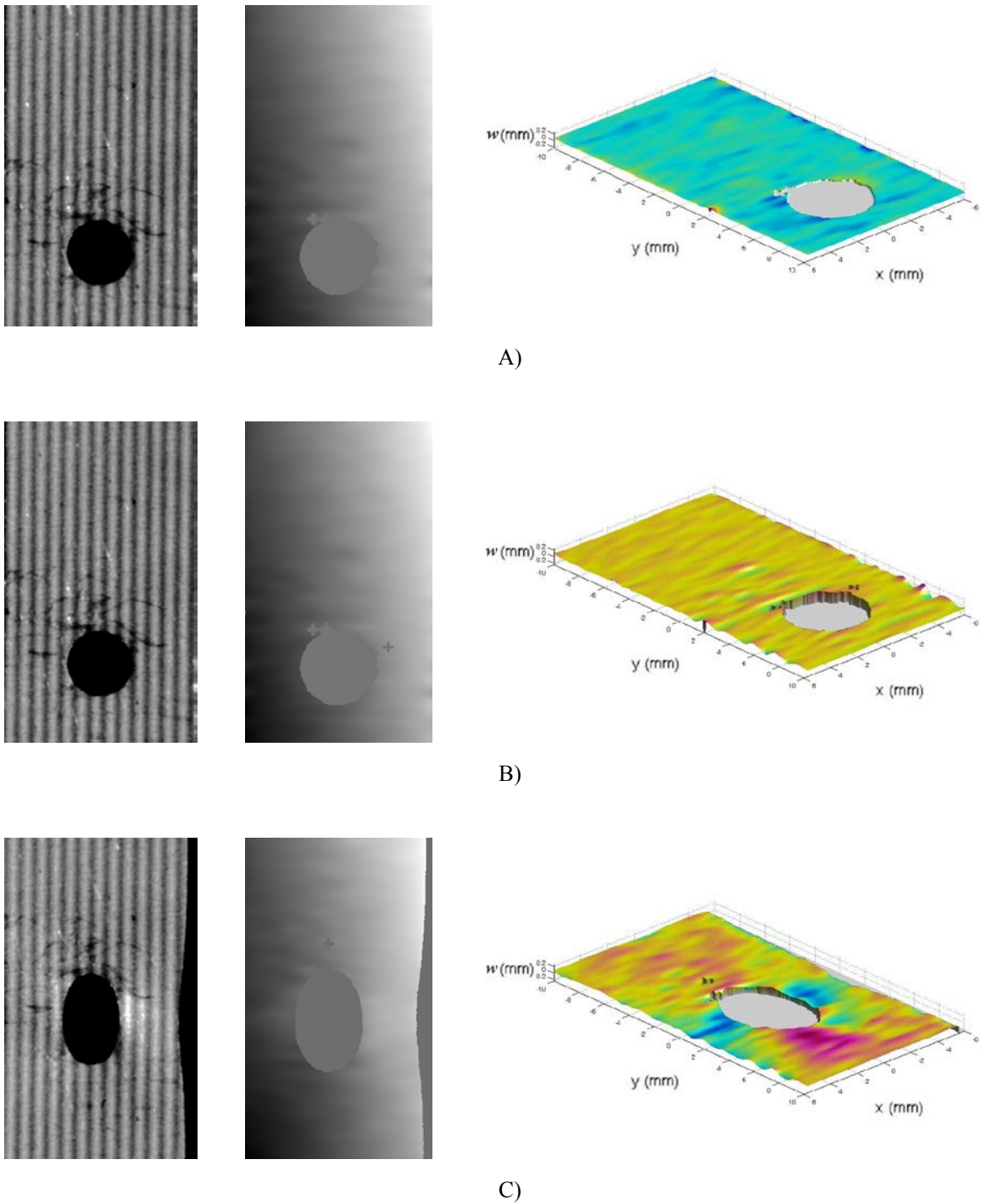
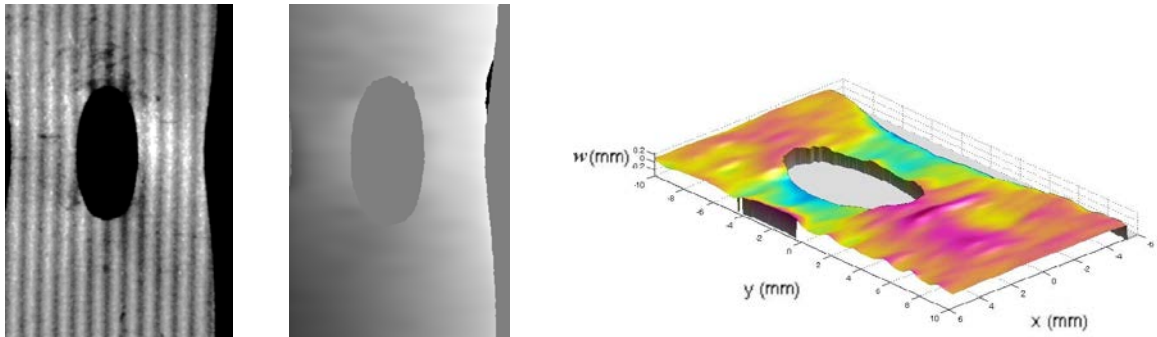
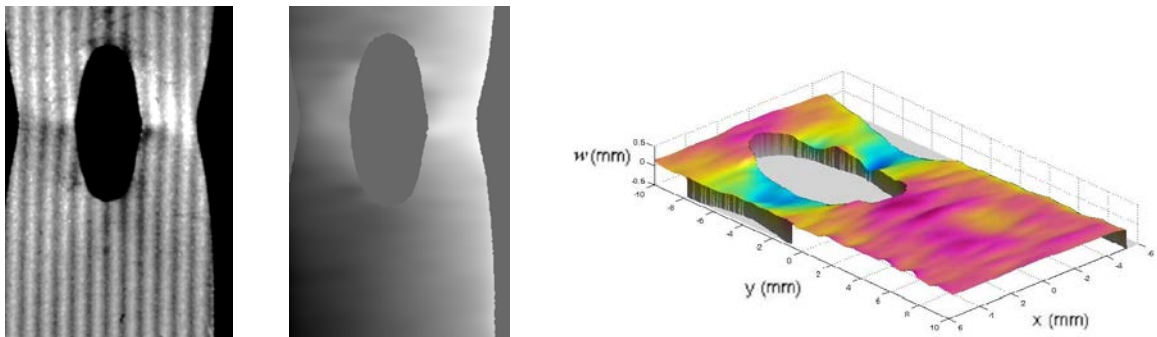


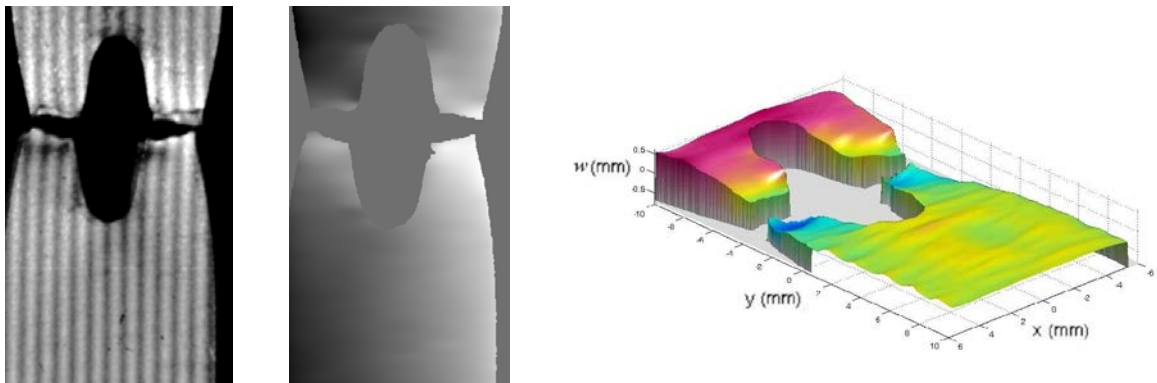
Figure 5.3 Fringe pattern, wrapped phase and deformation of the SS specimen during tensile test: A) beginning the test, B) elastic zone and C) plastic zone



D)



E)



F)

Figure 5.3 (Continued) Fringe pattern, wrapped phase and deformation of the SS specimen during tensile test:  
D) necking, E) before fracture, and F) fracture.

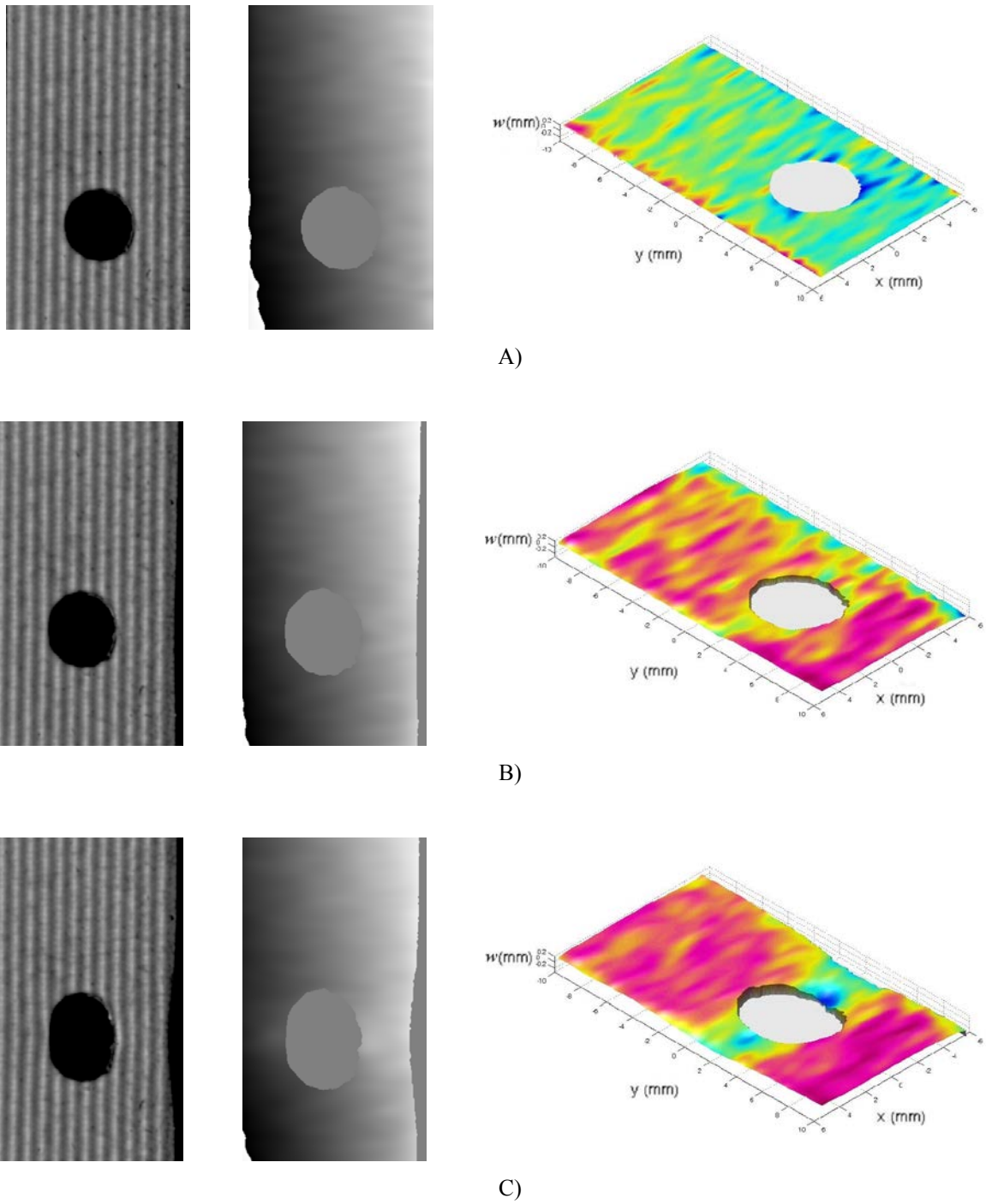
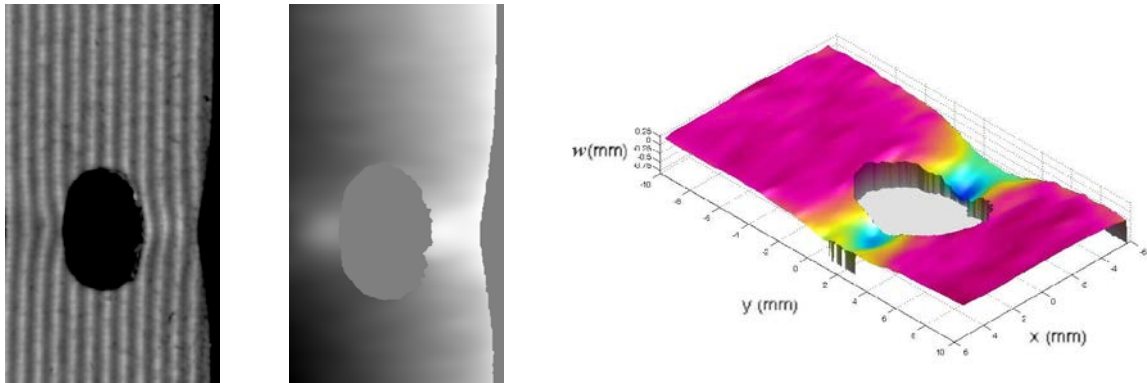
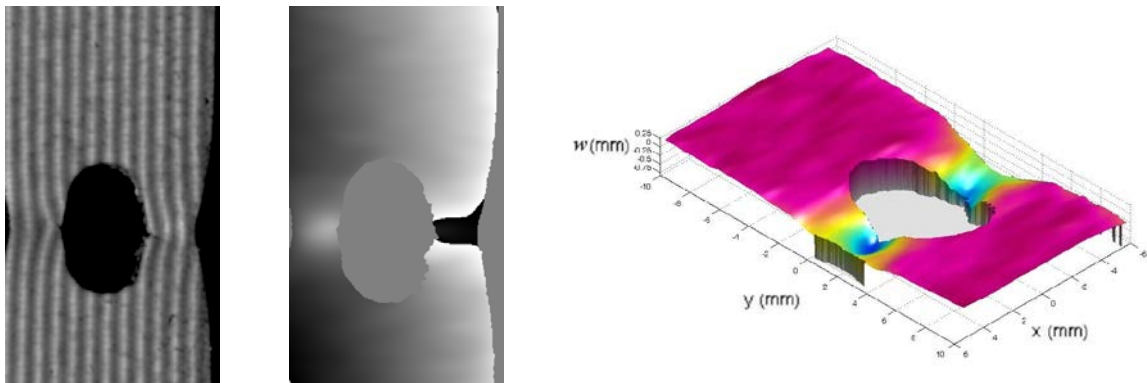


Figure 5.4 Fringe pattern, wrapped phase and deformation of the HRS C12 specimen during tensile test:  
A) beginning the test, B) elastic zone and C) plastic zone

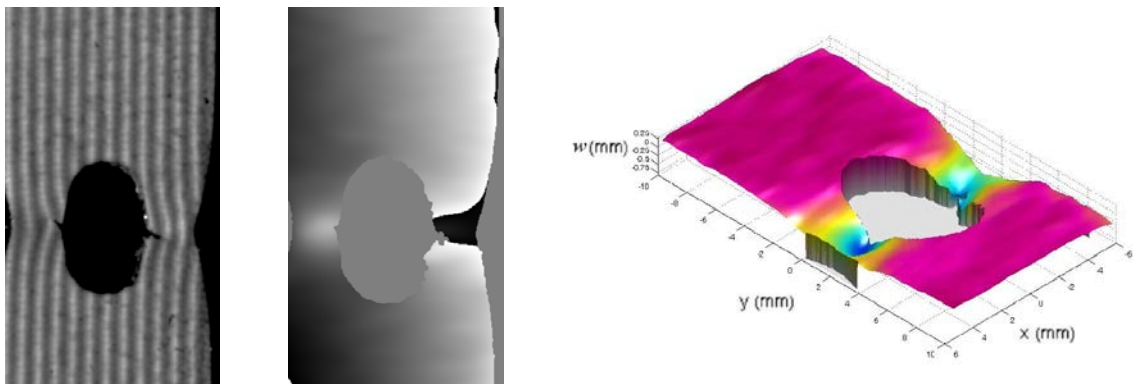




D)



E)



F)

Figure 5.4 (Continued) Fringe pattern, wrapped phase and deformation of the HRS C12 specimen during tensile test: D) necking, E) crack formation, and F) fracture progression.

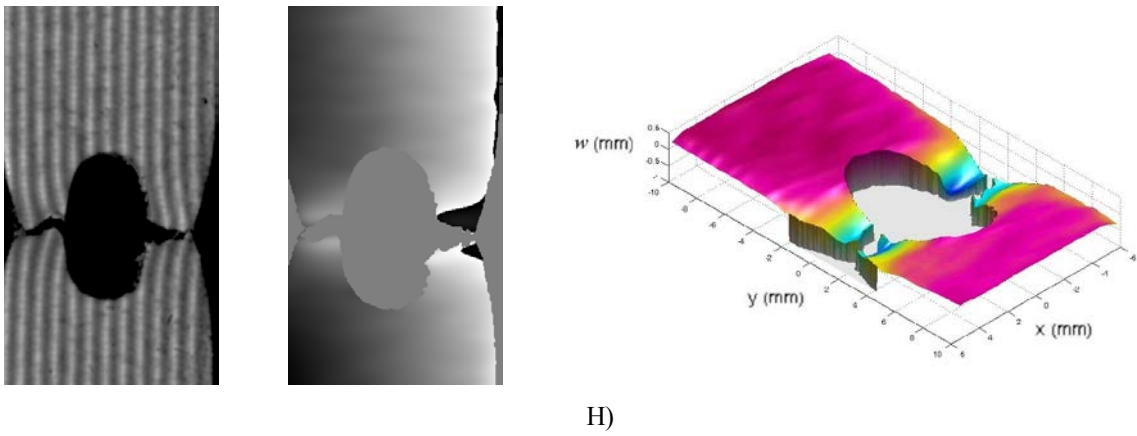
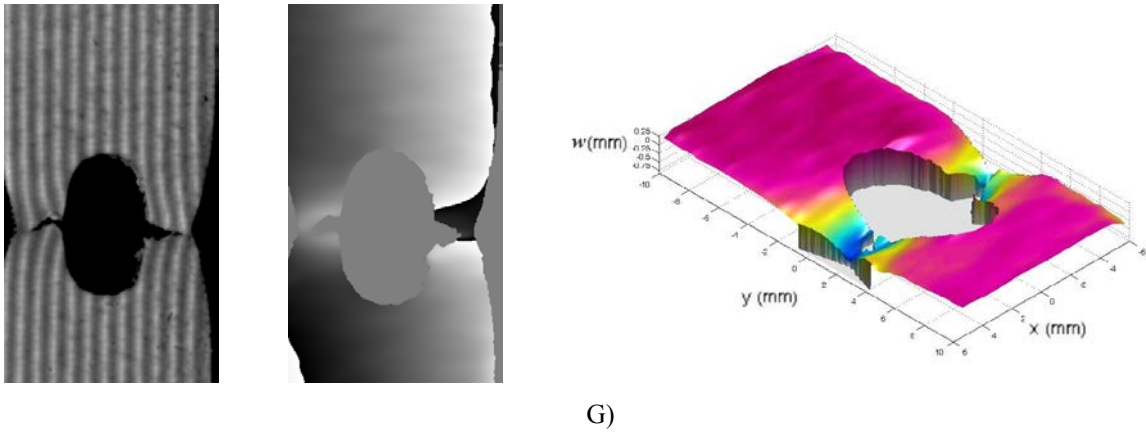


Figure 5.4 (Continued) Fringe pattern, wrapped phase and deformation of the HRS C12 specimen during tensile test: G) fracture progression and H) fracture.

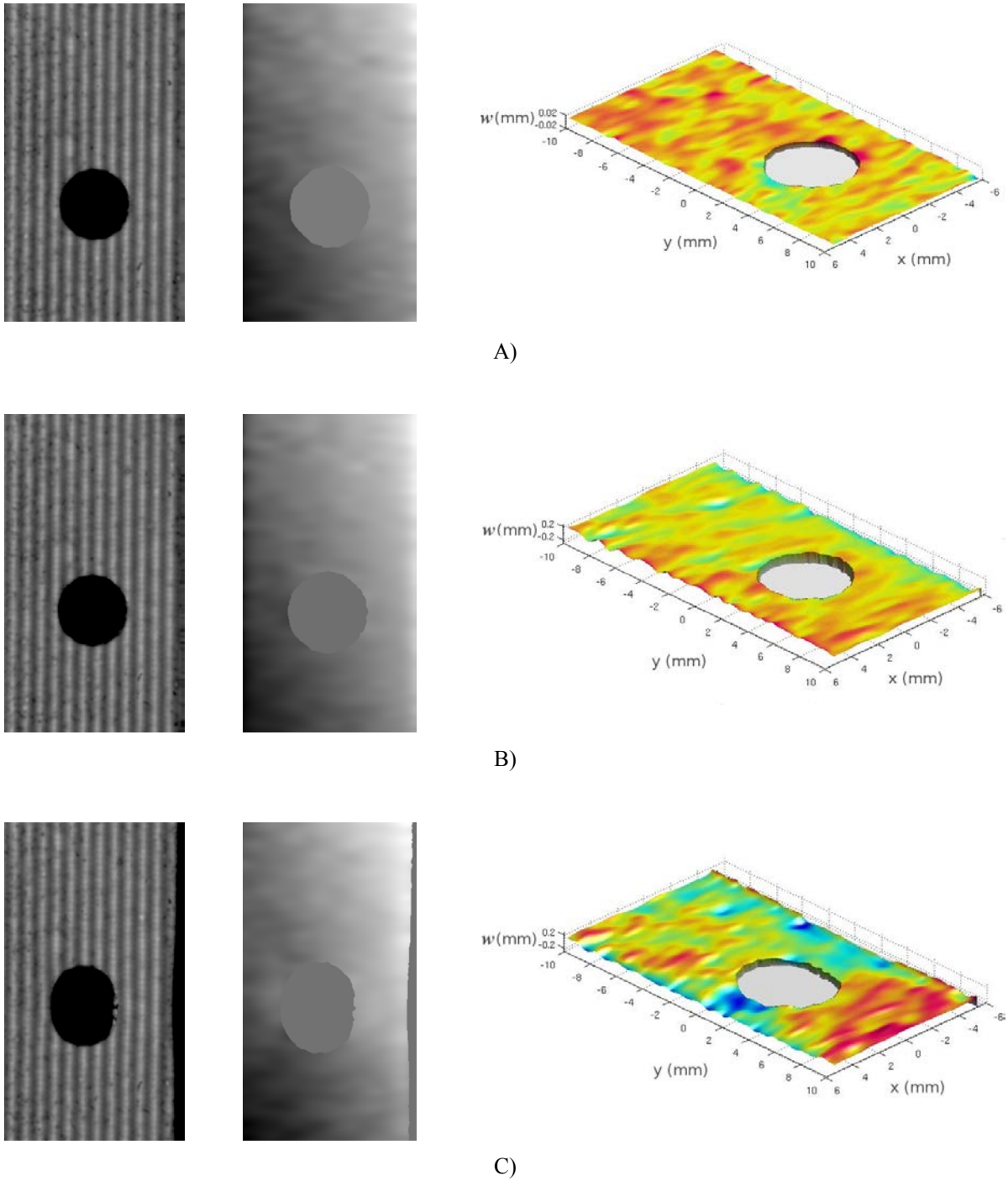
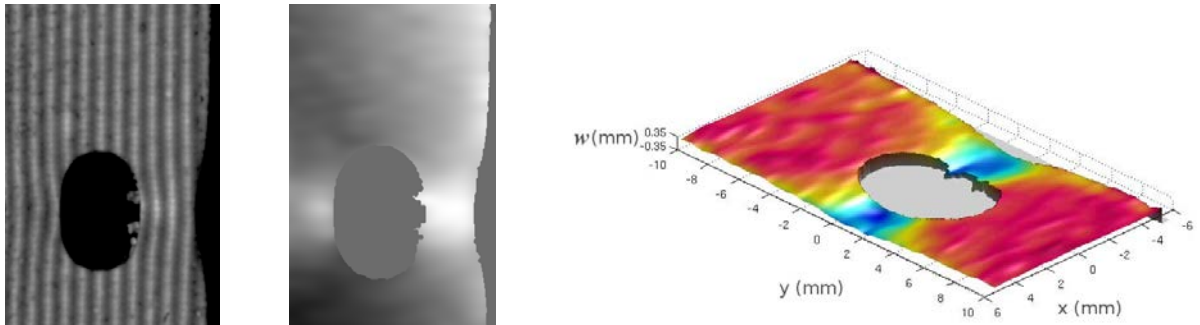
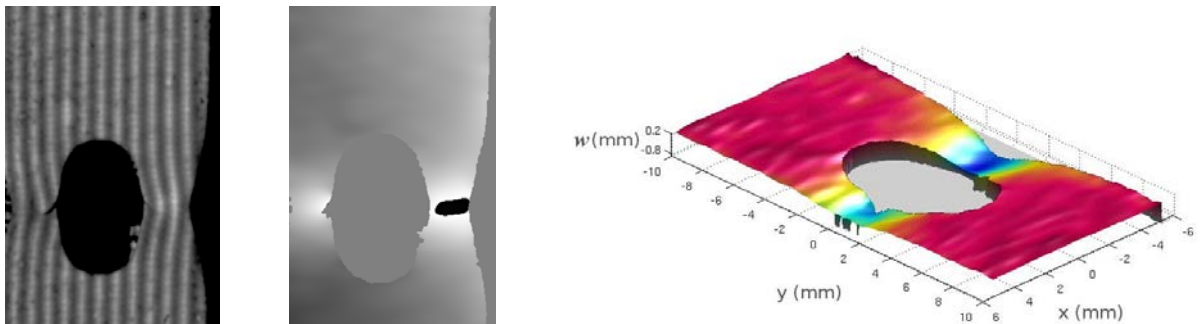


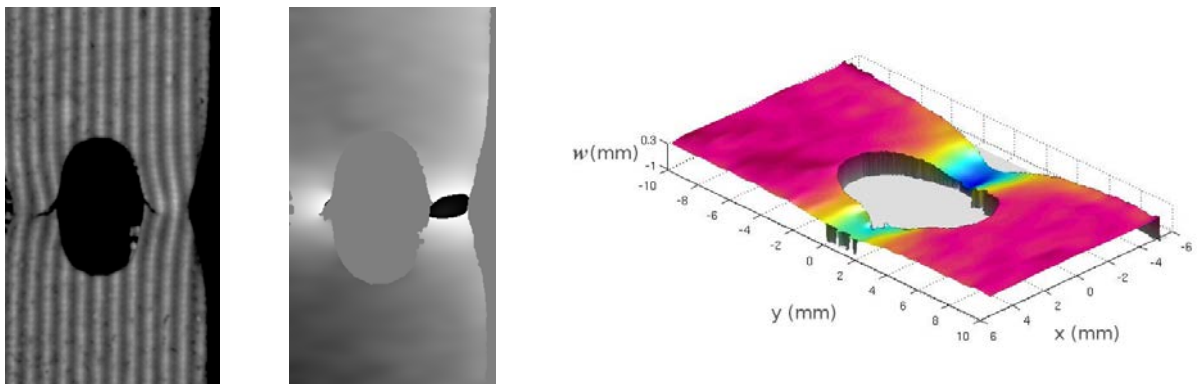
Figure 5.5 Fringe pattern, wrapped phase and deformation of the HRS C10 specimen during tensile test:  
A) beginning the test, B) elastic zone, and C) plastic zone.



D)



E)



F)

Figure 5.5 (Continued) Fringe pattern, wrapped phase and deformation of the HRS C10 specimen during tensile test: D) necking, E) crack formation, and F) fracture progression.

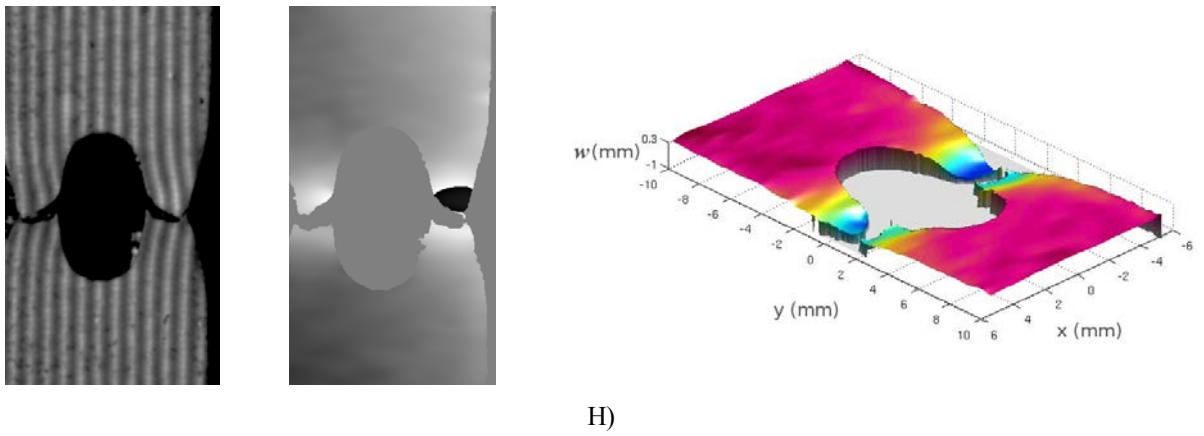
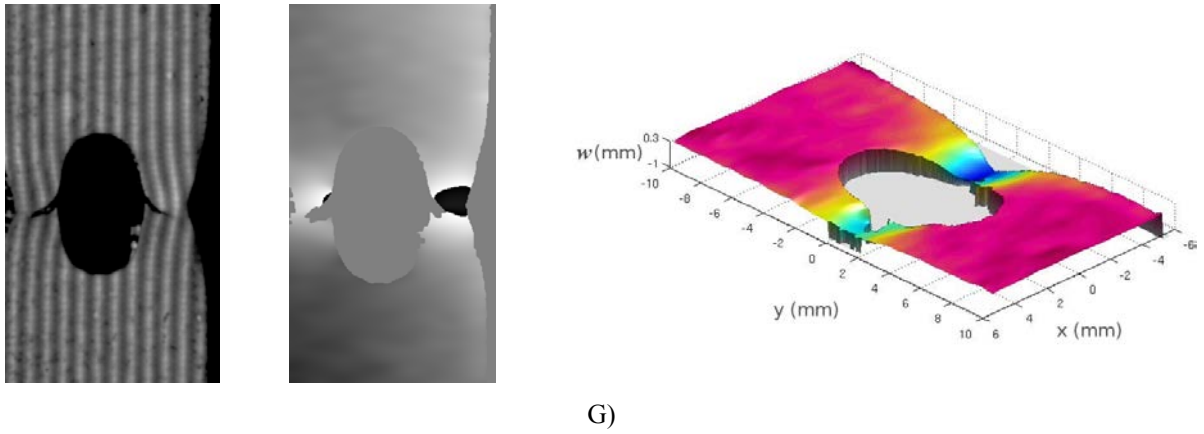


Figure 5.5 (Continued) Fringe pattern, wrapped phase and deformation of the HRS C10 specimen during tensile test: G) fracture progression and H) fracture.

### 5.3 CONCLUSION

We followed and reported [4] the deformation progression of sheet metal specimens of two different materials subjected to uniaxial tensile test by using fringe projection technique. By analyzing the out-of-plane displacements during the test, we observed that, during the transition zone, both materials began to thin along a horizontal band.

The detected behavior agrees with theory. The monitoring of the entire process allow us to compare the SS and HRS behavior. As mentioned above HRS specimens exhibited more necking and out-of-plane deformation while SS specimen shows higher elongation, as well fracture process of both materials is quite different as highlighted earlier.

The technique has potential application for dynamic measurement of deformation field of mechanical structures.

### REFERENCES

1. Anderson T.L., *Fracture Mechanics: Fundamentals and Applications*, CRC Press LLC, Boca Raton (1995)
2. Shukla A., Jain N., Chona R., “Dynamic fracture studies in functionally graded materials”, *Strain*, **43**, 76-95 (2007).
3. ASTM E8, “Standard Test Methods for Tension Testing of Metallic Materials (Metric)”, (2000)
4. León-Huerta A., Martinez Amalia, Rayas J.A., Cordero R., “Dynamic Measurement of Strain in Test Specimen by Fringe Projection”, in *Interferometry XIV: Techniques and Analysis*, Schmit J.; Creath K.; Towers C.E., Eds., *Proc. SPIE*, **7063**, 70631E (2008)

## CHAPTER 6

### FINAL CONCLUSIONS

---

All the contributions of this thesis work are enumerated in the following:

- We presented a bibliographic review of moiré methods and fringe projection technique, as well as a theoretical description of a few phase detection and phase unwrapping techniques used in the development of this work. During the realization of this thesis fringe projection technique was implemented to measure shape and deformation.
- We analyzed the error in the topography measurement by fringe projection technique when different grating periods are used. The use of CGGs allowed us to shift the phase via software, eliminating the possibility of phase shift errors. Has been showed how a nonsinusoidal fringe profile affects the shape measurement of an object, and the importance of determine the optimum period of the projected grating to adequately sample the object and minimizing the error in the result. From the obtained results we shown that an ideal grating period on the reference plane should be between *15-30 pix/fringe*. It was also mentioned the limitations associated with the configuration of the optical system. It was observed that the oblique illumination produces unwanted shadows that affect the results.
- We followed the deformation progression of sheet metal specimens of two different materials subjected to uniaxial tensile test by using fringe projection technique. By analyzing the out-of-plane displacements during the test, we observed that the detected behavior agrees with theory, and during the transition zone, both materials began to thin along a horizontal band due to the stress concentration in the edges of the hole drilled in the specimens. The monitoring of the entire process allow us to compare the behavior between two different materials due to their different mechanical properties. The main differences between both materials was the elongation, as well as the fracture process. It was possible by means of fringe projection technique to achieve the prediction of failure because that

deformations in transition zone were well detected.

- We determined that by using fringe projection technique any other material, as composites, or even manufactured members can be tested, through a nondestructive testing, due to the transition zone is successfully detected.

The future work is to apply phase shifting technique in real-time. The basic principle is to use a color pattern that is a combination of three phase shifted patterns. By using phase shifting technique any non full-field fringe pattern can be analyzed without fringe extrapolation.



## APPENDIX A: SPHEROMETER

A spherometer [1] is a mechanical device for measuring radius of curvature. The value of the radius is calculated by measuring the sagitta, Figure A.1. A classical spherometer consists of three equally spaced feet with central moving plunger. The spherometer is first placed on top of a flat surface and then on top of the surface to be measured. The difference in the position of the central plunger is the sagitta of the spherical surface. Several practical problems may arise. One is that sharp legs may scratch the surface, thus, a steel ball is placed at the end of the legs as well as at the end of the plunger (Aldis spherometer). In this case if the measured sagitta is  $z$ , the radius of curvature  $R$  of the surface is given by:

$$R = \frac{z}{2} + \frac{y^2}{2z} \pm r \quad \text{A.1}$$

where  $r$  is the radius of curvature of the balls. The plus sign is used for concave surfaces and the minus sign for convex surfaces.

The precision of this instrument may be obtained by differentiating Equation A.1, obtaining:

$$\Delta R = \frac{\Delta z}{2} \left( 1 - \frac{y^2}{z^2} \right) \quad \text{A.2}$$

This results is valid assuming that the spherometer is perfectly built and that the dimensional parameters  $y$  and  $r$  are well known. The uncertainty comes only from the measurement of the sagitta.

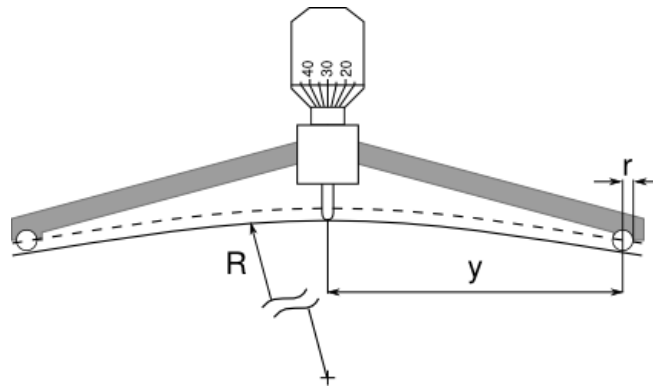


Figure A.1 Three-leg spherometer.

Another type of spherometer is the so-called ring spherometer, which has a cup instead of

three-legs. The cup is flat in the upper part and has its outside and external walls with a cylindrical shape, Figure A.2. A concave surface touch the external edge of the cup, whereas the convex surface touches the internal edge of the ring. Thus Equation A.1 may be used if a different value of  $y$  is used for concave and convex surfaces, and  $r$  is taken as zero. In this instrument the cups may be interchangeable, with different diameters for different surface diameters and radii of curvature. The main advantage is that an astigmatic deformation of the surface is easily detected, but it cannot be measured. With the three-leg spherometer the astigmatic deformations cannot be detected.

The spherometer accuracy may be improved in many ways, by different methods of taking the readings of the sagitta.

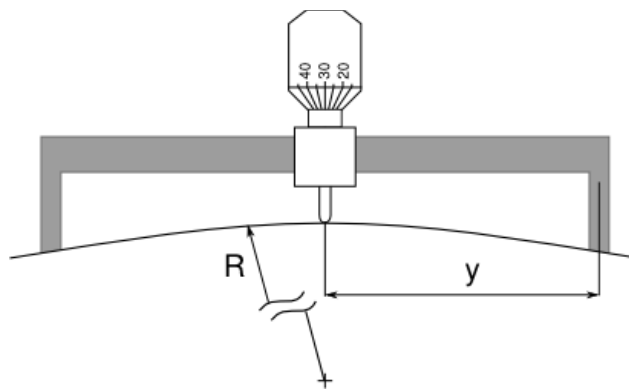


Figure A.2 Ring spherometer

## REFERENCES

1. Malacara J.Z., "Angle, Distance, Curvature, and Focal Length Measurements", *Optical Shop Testing*, Malacara D., Editor, Wiley, New York (1992)

## APPENDIX B: EXTRAPOLATION OF FRINGES

A non full-field fringe pattern can cause some errors in the phase detection, to avoid these errors fringe extrapolation outside the boundaries could be achieved [1] using the Gerchberg's method [2] as suggested by Roddier and Roddier [3]. To describe the intensity of a non full-field fringe pattern, Equation 3.4 must be multiplied by a function  $p(x, y)$  that describes the domain on which the interferogram extends, which a value of one inside the domain and a value of zero outside the domain. Then the intensity of the fringe patter can be written as:

$$g(x, y) = p(x, y)[a(x, y) + b(x, y) \cos(2\pi f_0 x - \phi(x, y))] \quad \text{B.1}$$

Now if we divide the irradiance by the background intensity and subtracts the domain we obtain:

$$g(x, y) = p(x, y)v(x, y)\cos(2\pi f_0 x - \phi(x, y)) \quad \text{B.2}$$

where  $v(x, y) = b(x, y)/a(x, y)$  represents the fringe visibility. If we use the complex fringe visibility,  $u(x, y)$ , defined by  $u(x, y) = v(x, y)e^{-i\phi(x, y)}$  in Equation B.2 we obtain:

$$g(x, y) = \frac{p(x, y)}{2} [u(x, y)e^{i2\pi f_0 x} + u^*(x, y)e^{-i2\pi f_0 x}] \quad \text{B.3}$$

The Fourier transform of the function  $g(x, y)$  is:

$$G(x, y) = \frac{P(f_x, f_y)}{2} * [U(f_x - f_0, f_y) + U^*(f_x - f_0, f_y)] \quad \text{B.4}$$

For a full-field fringe pattern, this spectrum would be concentrated in two circles with radii equal to the spatial carrier frequency of  $U(f)$  centered at  $f_0$  and  $-f_0$ . Due to the boundary, these circles increase in size as the domain decreases. Extrapolation of the fringes is easily achieved reducing the size of this two spots by cutting them around, setting to zero all the values outside these two spots and then taking the inverse Fourier transform. However, this process distorts the fringes a little, and to avoid this distortion, the original values are restored inside the domain. This process is repeated iteratively several times until the fringes are totally extrapolated outside the domain. Figure B.1 shows: A) A non full-field fringe pattern, B) the domain  $p(x, y)$  of the image and C) Full-field fringe pattern obtained.

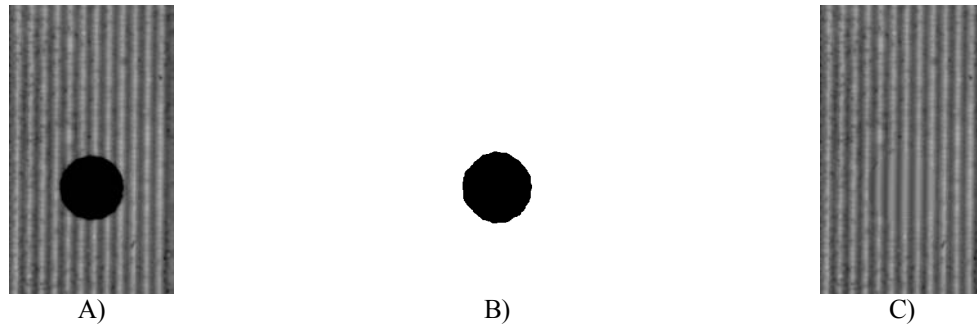


Figure B.1 A) Fringe pattern from a drilled specimen, B) Binary mask, C) Full-field fringe pattern obtained from fringe extrapolation.

## REFERENCES

1. Malacara D., Servin M., Malacara Z., *Interferogram Analysis for Optical Shop Testing*, Chapter 3, Taylor & Francis, Boca Raton (2005)
2. Grechberg R. W., "Super Resolution Through Error Energy Reduction", *Opt. Acta*, **21**, pp. 709-720 (1974)
3. Roddier C., Roddier F., "Interferogram Analysis Using Fourier Transform Techniques", *Appl. Opt.*, **26**, pp. 1668-1673 (1987)

## APPENDIX C: LIST OF WORKS PRESENTED IN MEETINGS

The results reported in this thesis were published in national and international conferences:

- **Conference Proceedings:**

1. **“Influencia del Periodo de Franjas Proyectadas en la Medición de la Topografía de Objetos”**

León-Huerta A., Martínez Amalia, Rayas J.A., Puga H.J.,

V Encuentro Participación de la Mujer en la Ciencia

21-23 May 2008 in León, Gto., México

ISBN 978-968-9241-04-1, S2-FMC T14

2. **“Dynamic Measurement of Strain in Test Specimen by Fringe Projection”**

León-Huerta A., Martínez Amalia, Rayas J.A., Cordero R.

SPIE Symposium on Optical Engineering + Applications

10-14 August 2008 in San Diego, CA, USA.

*Interferometry XIV: Techniques and Analysis*, Schmit J., Creath K., Towers C.E., Editors, *Proc. SPIE*, **7063**, 70631E (2008)

- **Meetings:**

1. **“Influencia del Periodo de Franjas Proyectadas en la Medición de la Topografía de Objetos”**

León-Huerta A., Martínez Amalia, Rayas J.A., Puga H.J.,

V Encuentro Participación de la Mujer en la Ciencia

21-23 May 2008 in León, Gto., México

2. **“Dynamic Measurement of Strain in Test Specimen by Fringe Projection”**

León-Huerta A., Martínez Amalia, Rayas J.A., Cordero R.

SPIE Symposium on Optical Engineering + Applications  
10-14 August 2008 in San Diego, CA, USA.

**3. “Medición Dinámica de la Deformación de Probetas Metálicas Usando Proyección de Franjas”**

León-Huerta A., Martínez Amalia, Rayas J.A., Cordero R.

LI Congreso Nacional de Física

20-24 October 2008 in Zacatecas, Zac., México.